

Validation of X-Band radar derived hydrodynamic phenomena

-MSc Thesis-

A. van Gils



Front cover: Sand Motor near Ter Heijde, Netherlands (source: Google Earth). This is an satellite image from August, 2013, 2 years after the completion of the Sand Motor, a large scale nourishment preventing the Dutch coast from erosion.

Validation of X-Band radar derived hydrodynamic phenomena

by

A. van Gils

in partial fulfillment of the requirements for the degree of

Master of Science
in Civil Engineering

at the Delft University of Technology.
to be presented publicly on Friday September 19, 2014 at 16:00 (CEST).

Thesis committee:	prof. dr. ir. M.J.F. Stive	Delft University of Technology
	dr. ir. P.B. Smit	Delft University of Technology
	ir. M. Henriquez	Delft University of Technology
	ir. R. Hoekstra	Deltares
	ir. C. Swinkels	Deltares

An electronic version of this thesis is available at <http://repository.tudelft.nl/>.



The work in this these was supported by Nortek. Their cooperation is hereby gratefully acknowledged.

Summary

The coastal area is a dynamic environment that suffers from human interventions and climate change. This requires extensive research and monitoring of the coastal areas. Measurement systems play a key role in the monitoring. Current velocities are for example often measured to investigate local hydrodynamics. At the moment the Acoustic Current Doppler Profiler (ADCP) is often used to measure current velocities. The disadvantage of this measurement system is the lack of spatial information. New innovative measurement systems are developed to overcome this disadvantage. The X-Band radar is an example of such a measurement system.

The radar signal reflects on the water surface resulting in images of the water surface. These images can be used to derive depth, current and wave information. The technique to do this was developed by (Young et al., 1985). A 3D Fourier Transformation is used to gain the wave information from the images. Subsequently the linear dispersion relation, which describes the fixed relation between wavenumber and wave frequency as a function of the depth and the current, is fitted through the obtained wave information to derive the depth and the current. This technique was further developed over the years and SeaDarQ is a contemporary algorithm that is able to derive depth and current from X-Band radar images. The output from this result is already researched by (Swinkels et al., 2012). This paper shows the potential of this algorithm as a measurement system. No description and validation of SeaDarQ is available. The accuracy of the output should be determined before this algorithm can be applied as measurement system. This aim of this study is therefore to investigate to what extent the SeaDarQ algorithm can be used to detect large scale hydrodynamic phenomena. Along the Dutch coast at Ter Heijde a mega nourishment is built, called the Sand Motor. This is a pilot project to research the feasibility to protect the Dutch coast from erosion with a mega nourishment. This project is closely monitored with a lot of conventional measurement systems such as the ADCP. This creates a great opportunity to validate SeaDarQ and therefore also a X-Band radar is placed near the Sand Motor.

To answer the main question, first the SeaDarQ algorithm itself is analysed to formulate several hypotheses about the limitations of the algorithm. Subsequently, these hypotheses are tested in a 2 week case study at the Sand Motor. In this case study one output point of the SeaDarQ velocity field is compared with ADCP data.

The SeaDarQ algorithm consists of several phases. In the first phase the reflections from other objects than waves are filter from the X-Band Radar images. A 3D Fourier Transformation is applied to gain the wave information from the images. Since the images are discrete

also the wave information is discrete and contains aliased components resulting from waves too short to capture in the images. These components are filtered from the algorithm. In the final phase the depth and current are determined in an iterative fashion. The depth is first estimated after correcting the wave information for the Doppler shift due to the current. Subsequently, the current is estimated after correcting the wave information for the intrinsic frequencies. The most important conclusion of this algorithm analysis is that not the same wave information is used for the depth and current fit. The longest waves are excluded from the current fit.

It can be concluded from the linear dispersion relation that the relative long waves are influenced by the depth and the current and the relative short waves (compared to the depth) are influenced by the current only. The current fit (which does not include the relative long waves) is therefore rather insensitive for the depth estimate. The case study indeed proved that a rough depth estimate is sufficient for a good current estimate.

Another consequence of excluding the relative long waves from the current fit is that the current is valid for the top part of the water column, since the short wave are only active in the top part of the water column. Comparison of the SeaDarQ data with different depth averaged surface currents measured with an ADCP revealed that the SeaDarQ output indeed compares the best with a 3.5 meter averaged surface current. This depth is probably not constant in time and space and more research into this depth is required.

In the case study also the influences of ambient conditions is investigated. The quality of the radar images and thus the quality if the wave information captured in the images is determined by the ambient conditions. The case study proved that a minimum of 2 m/s wind speed is required for accurate SeaDarQ output. During heavy rain, which contaminates the radar images, no SeaDarQ output is available. The 2 week case study includes a broad variance in ambient conditions. Different wind and wave directions were observed. The period includes calm periods with wave height of 28 cm till storm conditions with wave heights up to 5 meters. All these conditions proved to result in accurate SeaDarQ output. SeadarQ has also proven to give reliable current output during non-linear wave conditions and stratified conditions causing non-uniform velocity profiles.

It can be concluded that SeaDarQ is able to derive accurate velocities from X-Band radar images. This measurement device can be used in the future to derive and study complete velocity fields. The case study only included one spatial output point. For a proper validation this should be expanded to several output points to include the spatial variance of the output accuracy in the validation.

Table of Contents

Acknowledgements	vii
1 Introduction	1
1-1 Research Questions	2
1-2 Thesis Outline	2
2 Literature	3
2-1 Marine X-Band radar	3
2-2 Image Processing	5
2-3 Current Accuracy	7
2-3-1 Young 1985	7
2-3-2 Bell 2008	7
2-3-3 Hessner 2009	8
2-3-4 Swinkels 2012	8
3 SeaDarQ	11
3-1 SeaDarQ algorithm description	12
3-1-1 Preprocessing	12
3-1-2 Aliasing filter	13
3-1-3 Depth and Current estimate	16
3-1-4 Wave length and wave period estimate	19
4 Discussion	21
4-1 Input	21
4-2 Image spectrum	22
4-3 Depth and Current estimate	24
4-4 Line Fit	27
4-5 Influence ambient conditions	30
4-6 Influence hydrodynamic conditions	31

5	Two Weeks Case Study	33
5-1	Sand Motor	33
5-2	Data sets	34
5-2-1	Marine X-Band Radar	34
5-2-2	Acoustic Doppler Current Profiler	34
5-2-3	Metocean	36
5-3	Data analysis	39
5-3-1	Comparisson between ADCP and SeaDarQ	39
5-3-2	The influence of current fitting	41
5-3-3	The influence metocean conditions	44
5-3-4	The influence non-linear conditions	47
5-4	Spatial Analysis	50
6	Conclusion	53
7	Recommendations	55
	Bibliography	57

List of Figures

2-1	Modulation of capillary waves due to ocean waves	4
2-2	The backscatter intensities from one successive rotation of an X-Band radar located at the Dutch coast.	4
2-3	Radar wave image from Cape Cod, Massachusetts, 8 January 1976 from Mattie and Harris (1979).	5
2-4	Flowchart from algorithm developed by Young et al. (1985)	6
2-5	Energy density spectrum obtained by (Young et al., 1985)	6
2-6	Waterdepth and currents derived with the WaMoS II Algorithm at the Dee Estuary in Liverpool Bay	7
2-7	Radar derived bathymetry and velocity field for an flood current field and ebb current field	8
2-8	Time series of the water level, current speed and current direction from the research of Hessen and Bell (2009).	9
2-9	Comparison between SeaDarQ output and model output from a 2DH model at the Amelander inlet	9
2-10	Eddy formation and a fresh water plume captured in a X-Band radar image	10
2-11	Comparisson between SeaDarQ output and model output from a 2DH model at the Sand Motor	10
3-1	Image stack, named computational cube, from radar images	11
3-2	Flow chart of the SeaDarQ processing algorithm	13
3-3	Example of an energy density spectrum	14
3-4	Wide dispersion filter used to remove aliased components	15
3-5	Half of the spectral cube is removed to exclude aliased components.	15
3-6	The depth fitting procedure	16
3-7	The current fitting procedure	18
3-8	Example from Current fit from the SeaDarQ algorithm	19
3-9	Example from final linear dispersion relation fit	19
4-1	Influence of computational cube size on the energy density spectrum	22

4-2	Reflections from marker buoys in a radar image	23
4-3	Spreading of spectral contributions due to discrete data	24
4-4	Influence of depth and current on the shape of the dispersion shell.	25
4-5	Orbital movement induced by waves	28
5-1	Location of the measurement devices at the Sand Motor	34
5-2	X-Band radar and velocity output field from SeaDarQ	35
5-3	Acoustic Current Doppler Profilers	35
5-4	Extrapolation of the ADCP measurement data	36
5-5	Contour plot from ADCP measurement	37
5-6	Depth averaging of the ADCP data	37
5-7	Metocean conditions measured between 29th of November and 10th of December.	38
5-8	Scale scores for the SeaDarQ output compared with depth averaged ADCP data	39
5-9	Difference between SeaDarQ and ADCP output	40
5-10	Sensitivity of current direction with low flow velocities	41
5-11	Comparison between measured water depth and SeaDarQ depth output	42
5-12	Influence accuracy estimated depth on current accuracy	42
5-13	SeaDarQ compared with best depth averaged current output from ADCP for each time step	43
5-14	Influence wind speed on SeaDarQ output	44
5-15	Influence wind direction on SeaDarQ output	45
5-17	Influence wave height on SeaDarQ output	46
5-18	Influence of wave direction, compared to current direction, on SeaDarQ output	46
5-19	Velocity peaks due the fresh water plumes passing by at the Sand Motor	48
5-20	Fresh water plume observed in radar images at the Sand Motor	49
5-21	Line fit for the time step before and after the second sharp jump indicated in Figure 5-19. In both figure two currents seems to be visible.	49
5-22	SeaDarQ output compared to ADCP output during storm conditions	50
5-23	Hydrodynamics phenomena observed in SeaDarQ output	52

Acknowledgements

With this thesis I complete my study at the Delft University of Technology. It brought me a period of hard working, but also enjoyment. Although this is my thesis, I could not have write it without the help of others.

I would first like to acknowledge my committee for their support. Roderik and Cilia helped me keeping the overview of my work. Pieter supported me with the mathematics, making me enjoy Fourier Transformations and his critical reading improved my English writing. Martijn helped me structuring the information in this thesis. Marel Stive, my professor, provided several useful meetings wherein he helped me with the direction of my work.

Thanks also go to Javier for his patient in explaining me the SeaDarQ algorithm. The discussions and many mail conversations we had about SeaDarQ is the foundation of this thesis.

Next I would like to thank all the students at Deltares. We had a lot of fun together during the lunch and coffee breaks.

My family has been a great support during my work. Their faith in me helped me, especially during the difficult times. Special thanks go to my dad for reading and correcting my work. Finally I want to thank my boyfriend Luuk. His infinite faith in my ability to successfully complete this work has been very important to me.

Delft, University of Technology
September 8, 2014

A. van Gils

Chapter 1

Introduction

The impact of climate change and human interventions on coastal areas is assessed in coastal engineering. New harbours or harbour extensions and sea level rise are two examples that impact the coastal area. Development of harbours can be good from an economic point of view, but it has also a negative side regarding the environmental impact. Coastlines are retreating due to relative sea level rise, causing serious risk of flooding.

The interests of different stakeholders in the coastal area should be carefully balanced which is accomplished in coastal engineering. This includes monitoring which requires good measurements systems. The measurement data is used for direct analysis and as input for models to investigate the impact of, for instance a new harbour.

At the moment in-situ measurement systems are often used in monitoring. The wave buoy is for instance used to measure wave characteristics and the Acoustic Current Doppler Profiler (ADCP) provides current measurements. These systems have a couple of disadvantages: it is labour-intensive to place the systems in the water, the measurement systems often become damaged during storm conditions due to large forces in the water or by vessels sailing over the instruments and often no real-time data is available. Another disadvantage is the lack of spatial information. These measurement systems provide only data for one location. New measurement techniques are developed to overcome these disadvantages.

The X-Band radar is an example of such an innovative measurement technique. Images from the X-Band radar can be used derive depth, current and wave information. This technique overcomes the disadvantages of the measurement techniques mentioned in the first section. The most important advantage is the spatial information. The range of the radar is, depending on the elevation height, several kilometres. The radar can be positioned on land which makes it possible to provide real-time data and furthermore, the radar becomes less easily damaged. An algorithm is required to derive the depth, current and wave information from the radar images. An example of such an algorithm is SeaDarQ. This algorithm is currently owned by Nortek.

The Sand Motor is a pilot project that is built along the Dutch coast at Ter Heijde. This is a large scale nourishment in the shape of a peninsula, containing 20 million cubic meters of sand. The sand will spread due to natural processes, such as transport by currents, waves and wind, along the Dutch coast in 20 years. This nourishment replaces the yearly beach

nourishments that prevent the coast from eroding. The advantage of the large scale nourishment compared to the yearly nourishments is the smaller environmental impact. During the 20 years in which the Sand Motor will prevent the coast from erosion, no intervention is necessary which allows nature to develop. Another advantage is the recreation area it creates, which is suitable for walking, surfing and beach guests.

This pilot project is closely monitored including wave and current measurements from a wave buoy and two ADCPs. This creates a great opportunity to conduct research into the X-Band radar measurement technique and validate the output from SeaDarQ. A X-Band radar is therefore installed at the Sand Motor, beside the in-situ measurement techniques. The output of the SeaDarQ algorithm is already researched by (Swinkels et al., 2012). This paper emphasizes the potential of SeaDarQ as a measurement system. Unfortunately, no description and validation of the algorithm is available. The description is required to formulate hypotheses of the limitations of the algorithm. The validation is required to determine the accuracy of the output and test the limitations. This system can be applied to measure currents in the future, instead of a ADCP, if the validation reveals that the output is accurate.

1-1 Research Questions

The main research question is defined as:

- To what extent can SeaDarQ be used to detect hydrodynamic phenomena?

Three sub-questions are defined to elaborate this main question:

- How does the SeaDarQ algorithm derives the velocity from the X-Band images?
- Over which depth is the derived velocity valid?
- What are the limitations of the algorithm?

1-2 Thesis Outline

This thesis consists of two parts. In the first part the SeaDarQ algorithm is analysed in detail. This part is divided in two chapters: an analysis of the algorithm and a discussion. The first two sub-questions are answered in this part.

The collected data from the Sand Motor was analysed in the second part of this thesis. The SeaDarQ current output was compared with in-situ measurements to validate the output and determine the limitations of the algorithm.

Chapter 2

Literature

2-1 Marine X-Band radar

RAdio Detection and Raging (RADAR), is a remote sensing technique that is used to observe objects or phenomenon without making physical contact. This technique is commonly used for navigation purposes on vessels, air craft control and weather monitoring. Microwaves are emitted by the radar and the Doppler shift in time and space of the returned signal is used to infer intensity characteristics.

Sea surfaces can be monitored with a radar emitting microwaves in the X-Band segment (8.0-12.0 GHz). The return of the signal is either caused by specular reflection or by Bragg-resonant diffraction backscatter (Young et al., 1985). The specular reflection, which is a mirror like reflection, is most important at small angles of incidence and Bragg scatter is the important mechanism for larger angles of incidence (Valenzuela, 2012). The last mechanism is most important for land based radars. The Bragg-scatter criterion (Valenzuela, 2012) states that the microwaves reflect on waves with a wavelength half of the wavelength from the emitted signal. The wave length of the emitted wave is approximately 3 cm and it is therefore the high-frequency gravity capillary waves that causes the return of the radar signal. The ocean waves modulate the small capillary waves resulting in a difference in back scatter intensity (Valenzuela, 2012; Young et al., 1985; Borge et al., 1999, 2004). The large ocean waves can be studied indirectly from the reflected radar signal due to this modulation. Four types of modulations can be distinguished. These types are listed below and illustrated in Figure 2-1.

- Tilt modulation is caused by a local difference in angle of incidence.
- Hydrodynamic and orbital modulation both causes a grouping pattern in the capillary waves.
- Shadowing modulation is especially important for grazing incidence (large incidence angle). The higher waves hide the lower waves to the radar signal.

The wind speed, wind direction and range also influences the backscatter intensity (Borge and Soares, 2000). This intensity decreases for an increasing range. The intensity is also higher for larger wind speeds and wind blowing towards the radar.

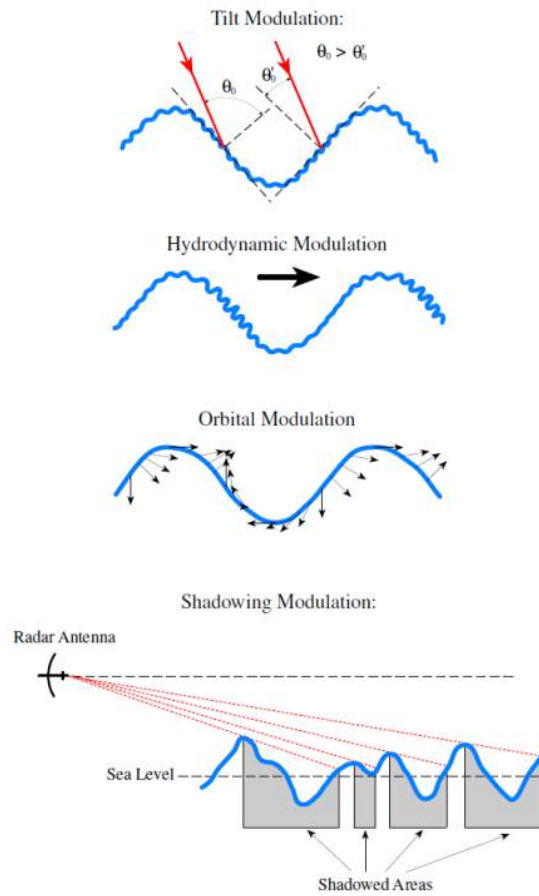


Figure 2-1: This image from Rutten (2013) illustrates the modulation of the small capillary waves due to the large ocean waves. These modulations result in a spatial difference in backscatter intensity. The long waves are indirectly visible in the radar images due to these modulations.

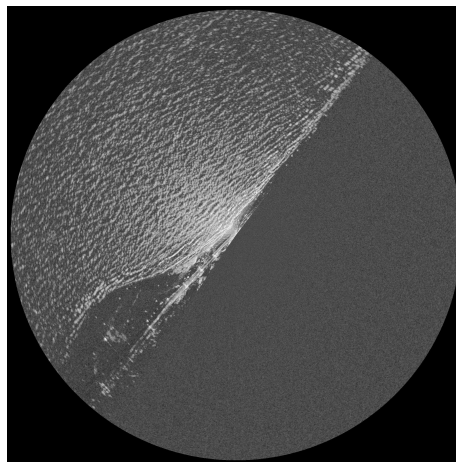


Figure 2-2: The backscatter intensities from one successive rotation of an X-Band radar located at the Dutch coast.

Figure 2-2 is an example of a radar image. The 360 degree view is obtained by rotating the radar after every emitted (and received) signal. Each image is the result of one successive rotation of the radar antenna. The temporal resolution of the radar images is limited by the rotation time of the antenna. The range resolution depends on the pulse length of the emitted signal and the azimuth resolution depends on the range and the beam width of the radar antenna.

2-2 Image Processing

The processing of radar images is developed over past decades. Mattie and Harris (1979); Oudshoorn (1960) visually inspected radar images to determine wave direction and wavelength. Figure 2-3 is a radar image from Mattie and Harris (1979) with marked wave trains.

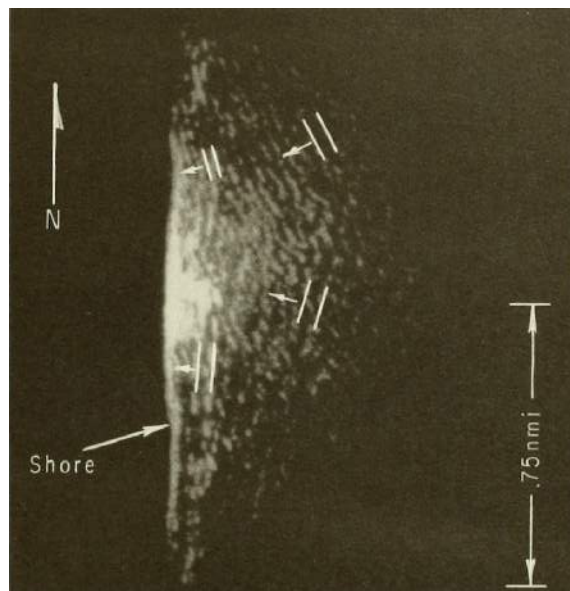


Figure 2-3: Radar wave image from Cape Cod, Massachusetts, 8 January 1976 from Mattie and Harris (1979). Two wave trains approaching the coast are marked in the image.

The processing technique of the radar images was further developed by digitizing the radar images and use 2D Fourier Transformation to extract a full wave spectrum (Ziemer et al., 1983). A 180 degrees directional ambiguity exists in the resulting spectra. The wave direction is determined by assuming that the wave direction is close to the wind direction. This approach only works for relative simple wave spectra.

The directional ambiguity can be solved also by using two radar images of the same area, separated by a short time interval (Atanassov et al., 1985). In this technique the linear dispersion relation is used, which describes the unique relation between wavelength and wave period. Young et al. (1985) further developed this technique by using a full time series of radar images to derive a three dimensional energy density spectrum $I(k_x, k_y, \omega)$ by using a 3D Fourier Transformation. Again the linear dispersion relation is used to derive the wave spectrum from the images. This technique is nowadays still used in algorithms to derive current, depth and wave information from radar images and is therefore described more extensively

below.

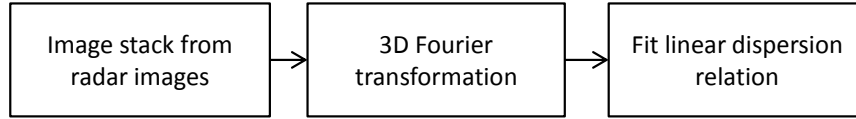


Figure 2-4: Flowchart from algorithm developed by Young et al. (1985)

A flowchart of the technique used by (Young et al., 1985) is presented in Figure 2-4. The process starts with selecting the image stack from the radar images. He used a rotating image such as described in the section above. From 32 consecutive images a square 128 x 128 pixels is selected and stacked on top of each other. This compares to a cube of 679 x 679 meter by 69 seconds. This image stack, named computational cube, is used as input for a full 3D Fourier Transformation. The output from this transformation is an energy density spectrum, $I(k_x, k_y, \omega)$. The linear dispersion relation, which describes the unique relation between wavenumber (k) and wave frequency (ω)

$$\omega = \sqrt{g|\vec{k}| \tanh|\vec{k}|d + \vec{k} \cdot \vec{U}}, \quad (2-1)$$

is fitted through the contributions. The three unknowns, Velocity in x direction (U_x), Velocity in y direction (U_y) and the depth (d) are solved. The location of the contributions in the energy density spectrum is an indication for the wave spectrum present in the radar images. Figure 2-5 shows the fit from an experiment executed by Young et al. (1985).

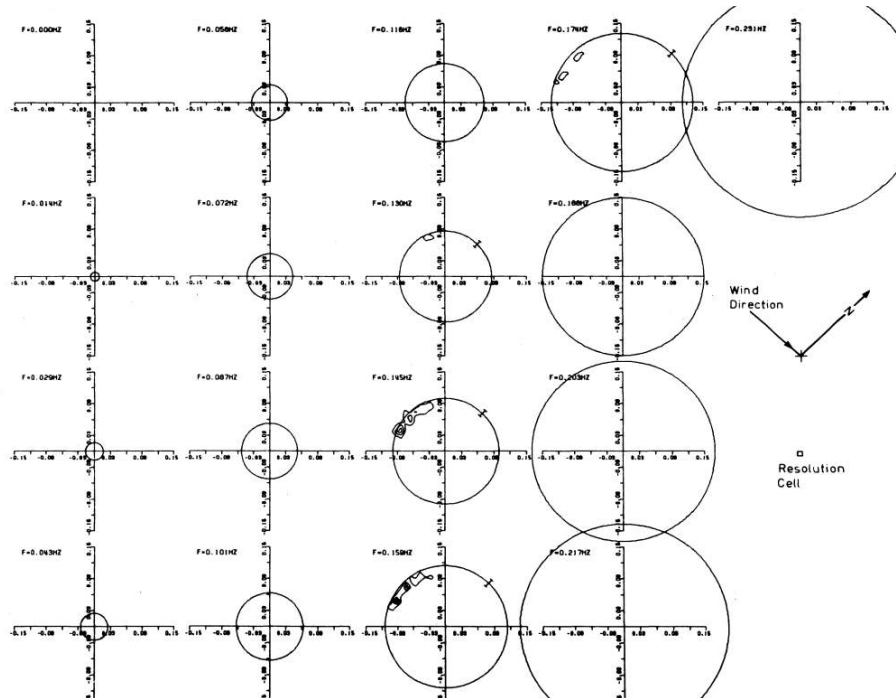


Figure 2-5: For the different frequency planes the contributions of the energy density spectrum obtained from the radar images are plotted together with the fitted dispersion relation. The contributions align very well with the fitted relation.

Nowadays two algorithms are available based on the principles presented by Young et al. (1985). The first algorithm was developed at the German GKSS Research Center and is named WaMoS II (Ziemer, 1991; Dittmer, 1995; Reichert et al., 1999). The second algorithm is owned by Nortek and is named SeaDarQ. No publications are available about this specific algorithm. This second algorithm will be analysed and validated in this thesis.

2-3 Current Accuracy

This thesis will focus on the current estimate from radar images. Several studies has been done on improving the current estimate and validation of the currents derived from radar images. In this section an overview is given from the work done so far.

2-3-1 Young 1985

Young carried out an experiment near the Island of Sylt on July 4, 1982 to test his algorithm. Measurements of one day were processed and analysed. To validate the current estimates a Aanderra current meter was deployed at 10.5m. depth. The algorithm using radar images derived a velocity of 0.64 m/s from 310°. The Aanderra meter measured a current of 0.45 m/s from 350°. It was also mentioned that the algorithm derives an average current near the surface. The measurement from the Aanderra current meter is corrected for this difference by using wind measurements, tide tables and taking the Ekman effect into account. The corrections resulted in a velocity of 0.69 m/s from 326° which shows surprisingly good agreement with the radar inferred values.

2-3-2 Bell 2008

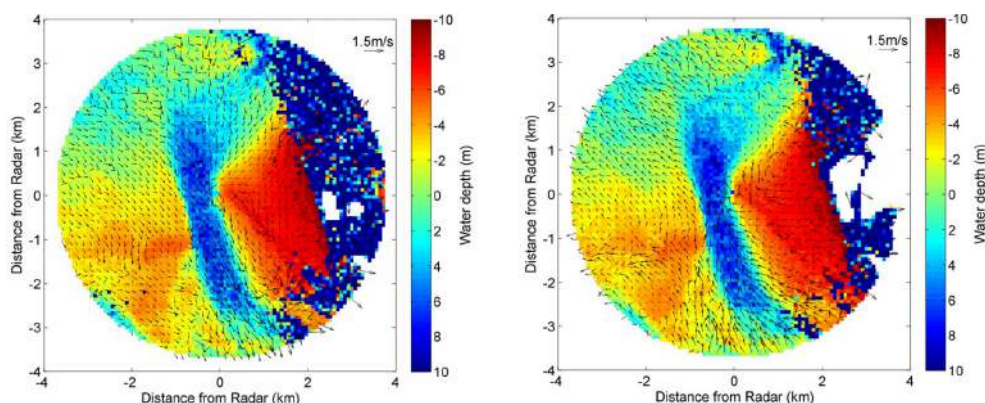


Figure 2-6: Waterdepth and currents derived with the WaMoS II Algorithm at the Dee Estuary in Liverpool Bay. The left plot is for a flood tide one hour prior to slack water and the right plot is for a ebb tide one hour after slack water.

Bell (2008) describes a measurement campaign of two days with a X-Band radar at the Dee Estuary in Liverpool Bay. The WaMoS II algorithm was used to derive wave, current and depth information from the radar images. The depth estimate is compared with surveys. No comparisons with independent current measurements have been made, but the improvement of the depth estimate by taking the current into account shows the potential of the current

estimate with a X-Band radar. Figure 2-6 shows to depth and current maps derived with the WaMoS II algorithm.

2-3-3 Hessner 2009

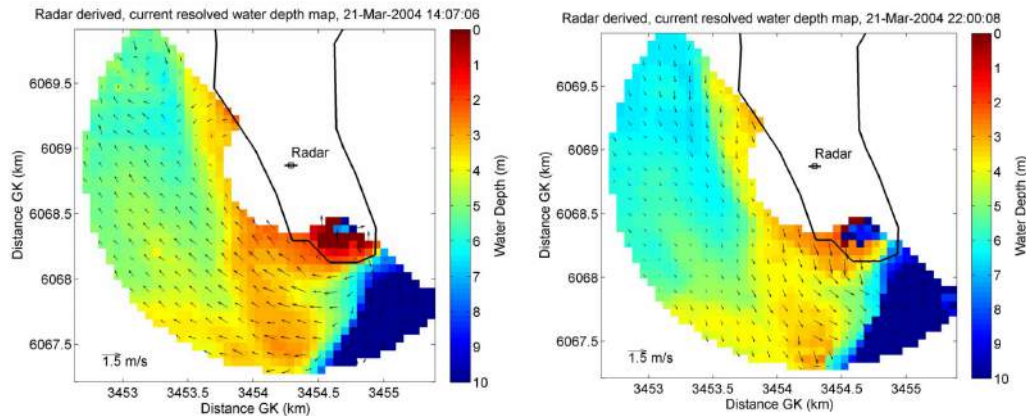


Figure 2-7: Radar derived bathymetry and velocity field for a flood current field (upper panel) and ebb current field (lower panel)

Hessen and Bell (2009) validated WaMoS II output on the basis of model output. The research area is located at the southern tip of the German Island Sylt. For validation a 3-dimensional model was used including waves, wave current interaction, water levels and density driven currents. The WaMoS II output is compared with 15 minutes averaged values in time and 3.2 km^2 in space for the upper 5 meter of the model. The computational cube with radar images was 128×128 pixels (0.36 km^2). The result for one point in space is plotted in Figure 2-8. Also high resolution current and bathymetry maps were derived. Figure 2-7 shows these maps for a flood current field and an ebb current field. It was concluded that WaMoS II is able to derive both wave and current parameters.

2-3-4 Swinkels 2012

Swinkels et al. (2012) validated SeaDarQ output on basis of model output for two test locations. The current output from both locations was compared with model results from a 2DH model. The first site is the Amelander Inlet, which is one of the tidal inlets between two barrier islands that separate the North Sea from the Dutch part of the Wadden Sea. Outliers in the radar derived velocities are correlated to certain conditions for this location.

- Strong gradients in bottom topography and current result in inhomogeneities in the computational cube whereby the algorithm does not converge
- Breaking of waves and white water bores disturbs the backscattering of the radar. The contributions in the energy density spectrum do not follow the linear dispersion relation in this case.
- The resolution of the radar images reduces at larger ranges which lowers the resolving capabilities of SeaDarQ.

Figure 2-9 shows two images of the model comparison. The model output is plotted in black and the SeaDarQ output in red. The RMSE was calculated for two days of comparison. The

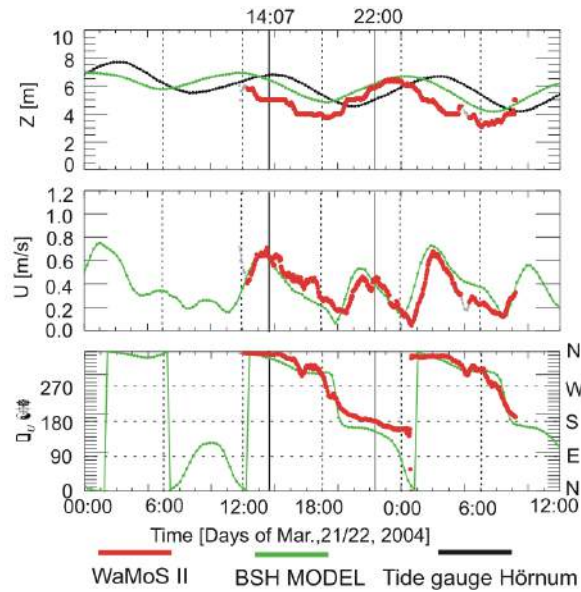


Figure 2-8: Time series of the water level (upper panel), current speed (middle) and current direction (lower panel) from the research of Hessner.

RMSE for the absolute velocity was 0.19 m/s and the RMSE for the velocity direction 30°.

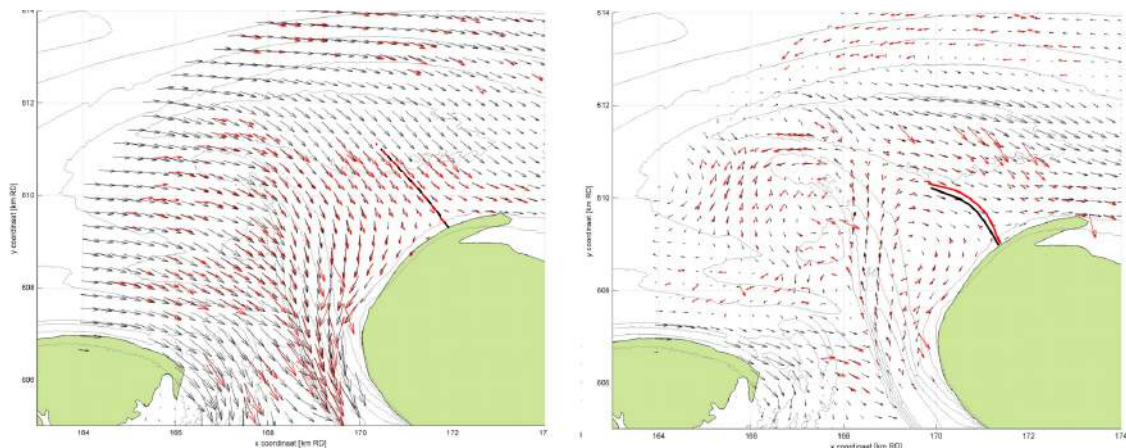


Figure 2-9: Comparison between SeaDarQ output and model output from a 2DH model. The model output is plotted in black and the SeaDarQ output is plotted in red. The left panel represents maximum flood flow and the right panel maximum ebb flow.

The second side is the Sand Motor which is a mega nourishment located along the Dutch coast at Ter Heijde. The SeaDarQ output for this location is also used for validation in this Thesis. The output is also compared with the output from a 2DH model although it is mentioned that stratification at this locations plays a signification role and for a fair comparison a 3D model should be used. First time averaged raw radar images were analysed. Due to the shape of the Sand Motor an eddy forms at the north side of the Sand Motor (Figure 2-10, left panel). The density current is also visible, in the radar time averaged images, as sharp edge (Figure 2-10, right panel). Figure 2-11 shows the model comparison for maximum flood and maximum ebb flow.

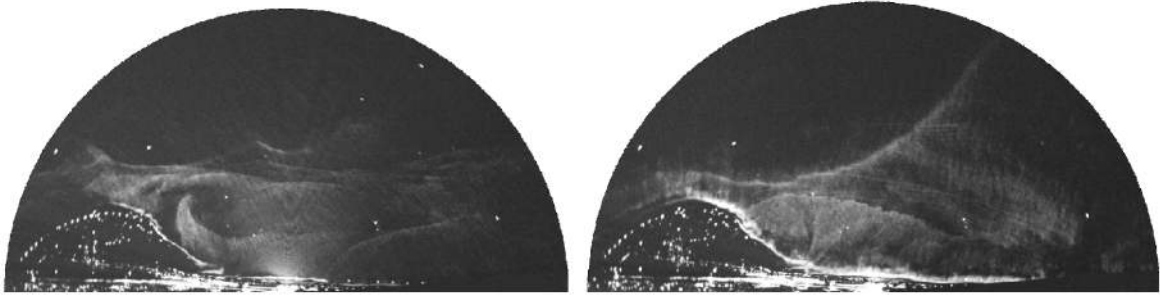


Figure 2-10: Time averaged radar images showing eddy formation at the lee side of the Sand Motor (left) and a fresh water plume passing by (right)

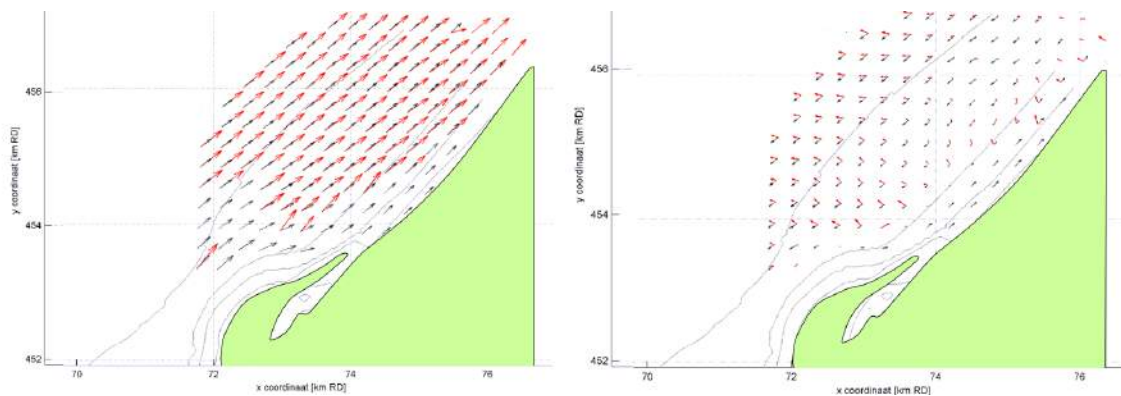


Figure 2-11: Comparisson between SeaDarQ output and model output from a 2DH model. The model output is plotted in black and the SeaDarQ output is plotted in red. The left panel represents maximum flood flow and the right panel maximum ebb flow.

Chapter 3

SeaDarQ

SeaDarQ is an algorithm that can be used to determine wave conditions, depth and current information from X-Band radar images. In this chapter a description of this algorithm is given¹. This description will help to understand the processes in the algorithm and pose a set of hypotheses with respect to the limitations and output validity of the algorithm.

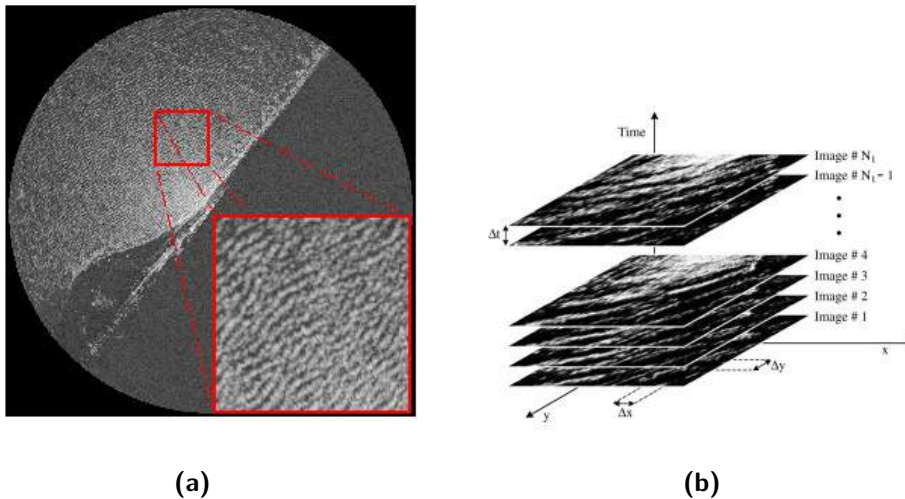


Figure 3-1: The left figure is a radar image from the Sand Motor with typical size of the computational cube indicated with a red square. The right figure illustrates an image stack of radar images (called computational cube) that is used to derive depth, wave and current information. (Borge et al., 2004).

Figure 3-1a shows a typical image obtained using the X-Band radar at the Sand Motor. This picture represents the intensity of the backscattered signal of the X-Band radar (Section 2-1). The shaded part of the image corresponds to the land half of the radar's field of view from which no reflected signal is obtained. The illuminated part of the image on the other hand

¹No literature, except a presentation from (Nortek, 2013), is available about this specific algorithm. The description is the result of several discussions with J. Perez, who currently manages the algorithm.

corresponds to the reflected signal from the sea surface. The rather sharp edge between these two regions corresponds with the coastline, where the curvature of the sand engine is clearly visible.

If we consider the illuminated part of the image in more detail (enlarged area Figure 3-1a), clearly a wave like pattern emerges. The radar signal is reflected by capillary wind waves that are modulated by the large ocean waves (Section 2-1). As a result, the ocean waves are captured in the radar images. In the remainder of this chapter it will be explained how depth and flow velocities can be obtained from these raw images.

3-1 SeaDarQ algorithm description

An image stack, named computational cube, of X-Band radar images is used as input for SeaDarQ. The computational cube effectively describes the intensity (denoted by $I(x, y, t)$) of the image at a set of discrete points in space and time. The spatial locations are captured by a discrete set of pixels in the image, and each successive image represents the advancement in time. This cube typically has a size of 256x256 pixels in x,y-space (≈ 1000 meter), indicated with a red square in Figure 3-1(a), and 64 frames in time (≈ 3.2 minutes). From 64 radar images, which are the result of 64 rotations from the radar antenna, the same square is selected. All these squares are stacked on top of each other. This is visualized in Figure 3-1(b). This computational cube is used to extract current, depth and wave information.

To extract this information the SeaDarq algorithm makes use of the fact that in the linear approximation, the frequency ω and wavenumber k of ocean waves are uniquely coupled to one-another by means of the linear dispersion relation, which reads,

$$\omega = \sigma + \vec{k} \cdot \vec{U} \quad (3-1)$$

where σ represents the intrinsic frequency,

$$\sigma = \sqrt{g|\vec{k}| \tanh |\vec{k}|d} \quad (3-2)$$

Consequently, considering the Fourier transform of the intensity function from (x, y, t) -space to (k, ω) -space it is expected that nonzero contributions collapse onto a dispersion shell corresponding to that of linear theory. These contributions can be obtained from the radar images by means of a 3D Fast Fourier Transform (FFT) resulting in a discrete energy density spectrum ($\hat{I}(k_x, k_y, \omega)$). Once this spectrum is obtained, the unknown depth and velocities can be obtained by searching for the best fit of the dispersion relation to these contributions.

To obtain this fit, the SeaDarq algorithm proceeds as indicated in the flow chart in Figure 3-2. Before the images can be transformed, preprocessing is necessary to remove noise from the images. Subsequently, the images are transformed and aliased components are removed after which the depths and currents are estimated in an iterative fashion. Each of the steps will be described in more detail in what follows.

3-1-1 Preprocessing

The goal of the preprocessing is to highlight the intensity differences due to reflections from waves. The reflections from buoys, ships and other objects are reduced with filtering techniques, because they will contaminate the energy density spectrum with contributions that



Figure 3-2: Flow chart of the SeaDarQ processing algorithm

are not concentrated along the dispersion plane. Moreover, the preprocessing stage also determines the quality of the images with regard to the visibility of the waves. Especially for low waves (e.g. low wind conditions), the contrast between the illuminated and shadowed parts of the image is low and no clear wave pattern can be discerned. To determine whether or not the image has sufficient contrast, the SeaDarQ algorithm determines the standard deviation of the image, and only proceeds if the standard deviation of the intensity (a measure of the contrast) exceeds 0.3, otherwise the image is rejected.

The average intensity of the computational cube is removed first since the waves show up in the intensity differences. The time average intensity is removed to reduce the contribution of reflections from marker buoys and other solid objects. A 3D Hamming filter, (Allen, 1977) is applied before performing a 3D Fast Fourier Transformation (FFT) to reduce the spectral leakage. The 3D FFT is applied which is a FFT in three directions. The transformation, implemented in (Matlab , 2014), that is used in SeaDarQ, is given below. The full transformation is given for x to k_x space.

$$G_1(k_x, y, t) = \mathcal{F}_{x,k_x}\{I\} = \sum_{x=1}^N I(x, y, t) e^{-\frac{2\pi i}{N}((x-1)(k_x-1))} \quad \text{for } x = 1 : 256 \quad (3-3)$$

The transformations from y to k_y and from t to ω are performed similarly,

$$\begin{aligned} G_2(k_x, k_y, t) &= \mathcal{F}_{y,k_y}\{G_1\} \\ \hat{I}(k_x, k_y, \omega) &= \mathcal{F}_{t,\omega}\{G_2\} \end{aligned} \quad (3-4)$$

The energy density spectrum ($\hat{I}(k_x, k_y, \omega)$) that is obtained after performing the FFT, is normalized to get an even distribution of the spectral energy over the dispersion shell.

Figure 3-3 shows an example such a spectrum

3-1-2 Aliasing filter

Due to the relative long rotation time of the radar (3 seconds) compared to typical wave periods (4-12 seconds), temporal aliasing occurs in the signal. This rotation-time results in a sampling frequency of 0.33 Hz. The shortest wave which can be observed is, according to the Nyquist limit, 1.5 seconds. All waves shorter than this limit show up in the energy density spectrum as longer waves. This phenomenon is called aliasing. This aliased components, pointed out with red circles in Figure 3-3, needs to be removed to be able to fit the dispersion relation, because these components do not concentrate on the sheared dispersion shell.

The first step in the aliasing removal process is the application of a wide dispersion filter. This filter removes all contributions below and above certain estimates of the dispersion plane and is built from the linear dispersion relation (3-1) with fixed upper and lower limits for the depth

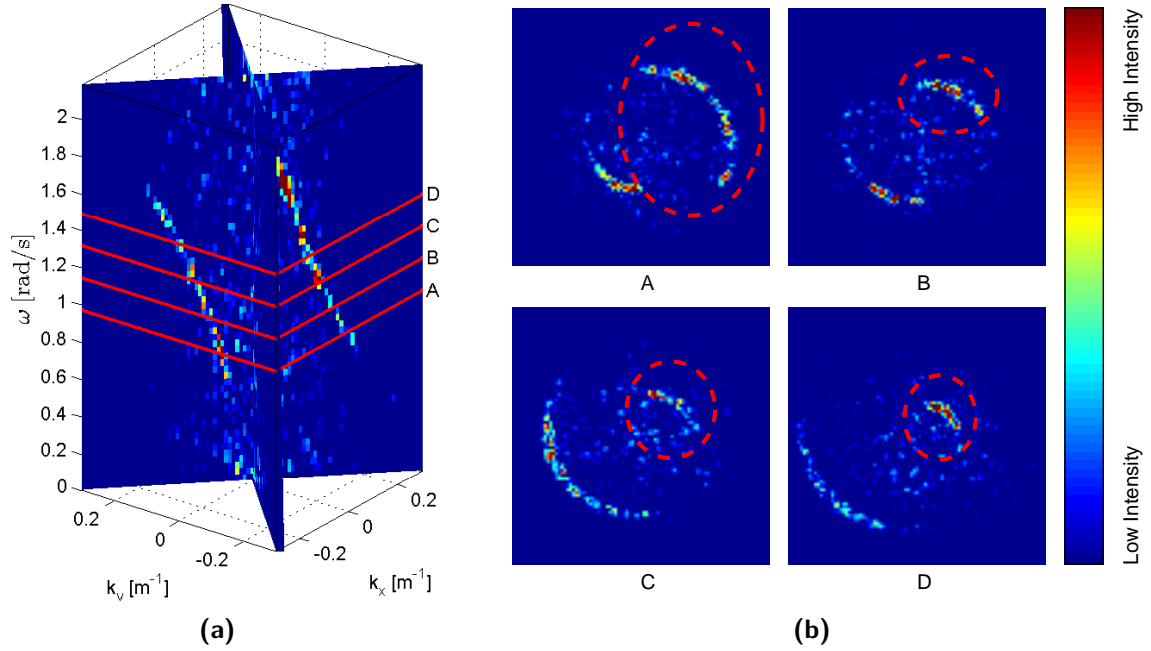


Figure 3-3: Figure (a) shows two slices of the spectrum that is obtained after the preprocessing. Colors indicate how strong wave-components are present in the image cube. The four red slices that are marked in the left figure are plotted in Figure b. In this figure the aliased components are marked with red dashed circles.

and the current. The default settings for these parameters are: $d_{min} = 5m$, $d_{max} = 100m$ and $U_{max} = 2m/s$, for which no formal justification is given. The boundaries are defined as: $\omega(d_{min}, -u_{max})$ and $\omega(d_{max}, u_{max})$ were ω . The removed components are indicated in gray in Figure 3-4.

The aliased components always lie in the opposite direction of the actual components; this is used to filter these components from the energy density spectrum. The remaining energy density spectrum is transformed to polar coordinates,

$$\hat{I}(k_x, k_y, \omega) \xrightarrow{\text{polartransform}} \hat{I}(k_r, k_\theta, \omega) \quad (3-5)$$

and summed over the wave-numbers and frequencies,

$$\sum_{k_r, \omega} \hat{I} = \hat{I}(k_\theta) \quad (3-6)$$

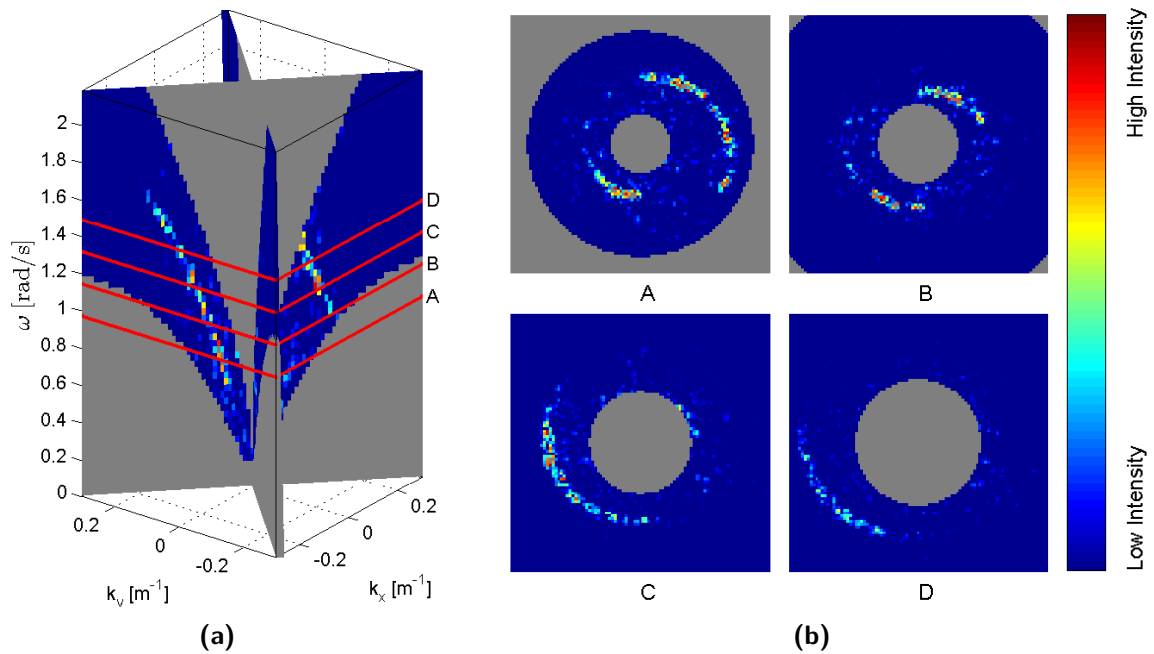
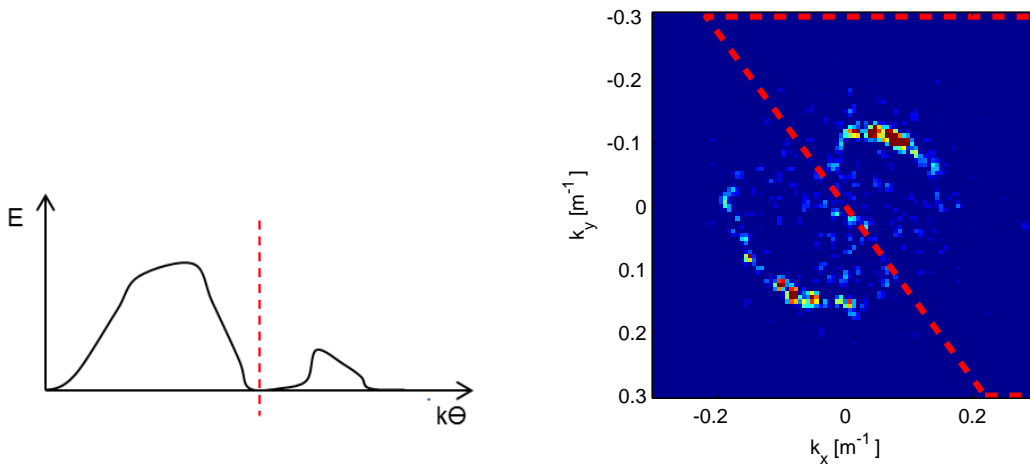


Figure 3-4: Figure a shows the energy density spectrum with in gray the wide dispersion filter which is applied in the first step to remove the aliased components. The four omega-planes indicated in red are plotted in Figure b.



(a) A schematic view of the energy density spectrum after the transformation to polar coordinates and the summation over k_r and ω . In the red the direction with minimum energy is indicated.

(b) This Figure shows one omega plane in which with a red dashed line the side of the cube is indicated which will be removed. The other side of the cube remains and is used for the depth and current estimate.

Figure 3-5

This results in an intensity distribution over the wave directions which is schematically plotted in Figure 3-5a. Two energy peaks are found, one belongs to the components which lie on the sheared dispersion shell and the other peak belongs to the aliased components. In most cases part of the contributions of the aliased components are removed with the wide dispersion filter

which results in a lower energy peak for these components. The separation angle between both peaks is determined at the angle with the minimal energy.

If the contributions of the aliased components all lay inside the wide dispersion relation no smaller energy peak is found for these components. In this case the algorithm is not able to decide which side of the spectrum to remove and no current, depth and wave estimate will be available

The aliased components are removed from the original spectrum in Cartesian coordinates based on the separation angle and side (Figure 3-5b). The remaining half of the spectral cube is used for the depth and current estimate which will be explained in the next section.

3-1-3 Depth and Current estimate

The depth and current are estimated from the energy density spectrum, which remains after the aliasing removal, in an iterative process. Initially the current is set to 0. Next, the algorithm proceeds in an iterative fashion to obtain a new depth estimate. The Doppler contribution is subtracted first from the coordinates of the non-zero contributions of the spectrum using the most recent current estimate. Subsequently the depth is estimated by fitting the intrinsic frequency (3-2) to the data. Then, using the newly acquired depth estimate, the intrinsic frequency contribution is subtracted from the coordinates of the non-zero contributions of the spectrum, and the Doppler term is fitted to the coordinates of the non-zero contributions, thus obtaining a new estimate for the current. This process is repeated 3.5 times (ending with a depth estimate) and it is assumed to have converged. Each step in this process will now be discussed in detail.

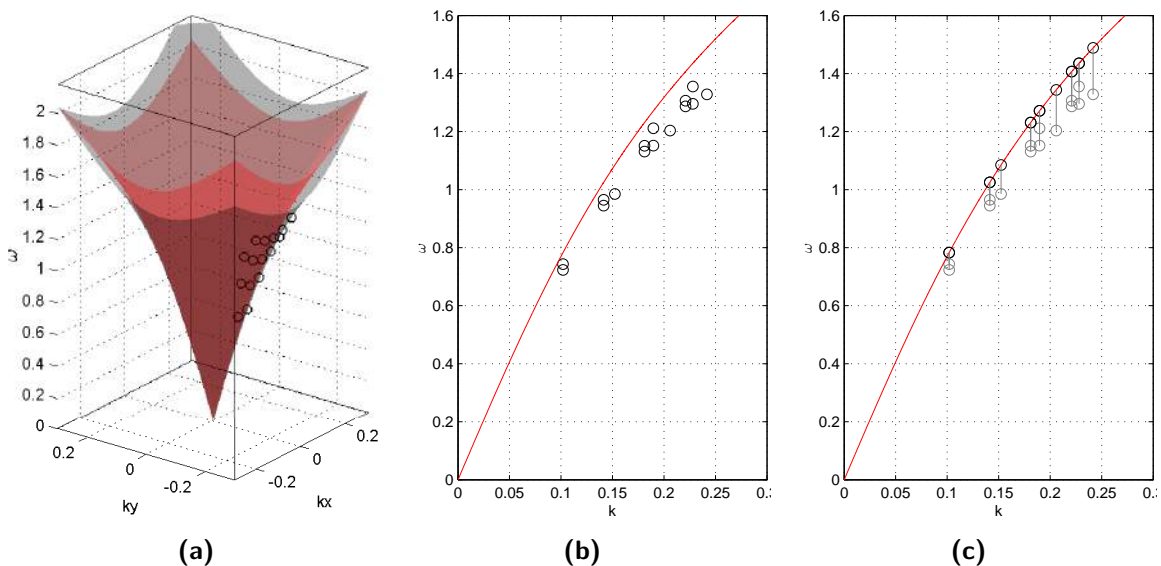


Figure 3-6: Figure a shows in black the complete dispersion shell for $d = 7$ meter, $U_x = 0.5$ [m/s] and $U_y = 0.5$ [m/s]. In red the dispersion shell without a current is plotted. The black dots in this figure represent some spectral data which is used for illustration. In Figure b the data is plotted in 2D, which contains no directional information anymore. The red line is the searched dispersion shell without current. Figure c illustrated the ideal case were the current is compensated correct which moves the spectral data to the searched dispersion shell.

The depth estimate starts with the current compensation,

$$\omega_{new} = \sigma + \vec{k} \cdot \vec{U} - \vec{k} \cdot \vec{U}_{estimate} \quad (3-7)$$

In the first iteration when no current estimate is available $U_{estimate} = 0$ is used. Figure 3-6a shows the deformation of the dispersion shell due to the presence of a current. When the current is compensated correctly ω_{new} will not contain any deformation due to the current anymore which results in a symmetric dispersion shell with respect to the ω -axis. The black circles in Figure 3-6a indicate the data points that are used to illustrate the steps in the algorithm to come to a depth estimate.

After the current compensation a wide dispersion filter is applied to make a first rough selection of the contributions in the energy density spectrum which possibly belong to the dispersion relation. The boundaries of this wide dispersion relation are the same as the ones used for the aliasing removal: $\omega(d_{min}, -u_{max})$ and $\omega(d_{max}, u_{max})$ where ω is the linear dispersion relation.

The presence of a current bends the shape of dispersion shell. The intrinsic shell remains when the spectrum is compensated for the current correctly. The remaining intrinsic dispersion shell is symmetric with respect to the ω -axis. This symmetry is used in the depth estimate.

The remaining contributions in the energy density spectrum are transformed to polar coordinates and summed over the directions. All the directional information is removed in this way. The data can now presented in 2D. In Figure 3-6b the data is plotted after this transformation and summation. The red line indicates the intrinsic dispersion shell that is obtained after the correct current compensation. This is the searched dispersion relation for the depth estimate. The black circles indicate the original data point without correction for the current. The points are spread due to the influence of the current that bends the shape of the dispersion shell.

When a reasonable current estimate is available, after some iterations, the data points will move to the searched red dispersion relation. Figure 3-6c shows the result after a compensation for exact the right current.

The depth is estimated by fitting the intrinsic dispersion shell 3-2, through the spectral contributions of the energy density spectrum in k, ω -space. The Leven-Marquart algorithm Press et al. (1986), which is a least-square fitting algorithm for non-linear problems, is used to fit the intrinsic dispersion shell. This results in a (new) depth estimate. The maximum number of iterations for this Leven-Marquart algorithm is set to 20. If no convergence is reached after 20 iterations no depth estimate will be available.

In the next step a current estimate is made. This process starts again with the energy density spectrum which is obtained after the aliasing removal. A wide dispersion filter like for the aliasing removal and the depth estimate is applied first. For this filter the estimated depth is used to determine the boundaries: $\omega(d_{estimate}, -u_{max}), \omega(d_{estimate}, u_{max})$. If no depth is available the same boundary conditions as for the depth estimate are used

The remaining contributions from the energy density spectrum are compensated for the depth term of the dispersion relation,

$$\omega_{new} = \sigma + \vec{k} \cdot \vec{U} - \sqrt{g|\vec{k}| \tanh |\vec{k}| d_{estimate}} \quad (3-8)$$

Figure 3-7a shows the total dispersion relation in black and the dispersion relation compensated for the depth term in red. Again in black circles spectral contributions are plotted that

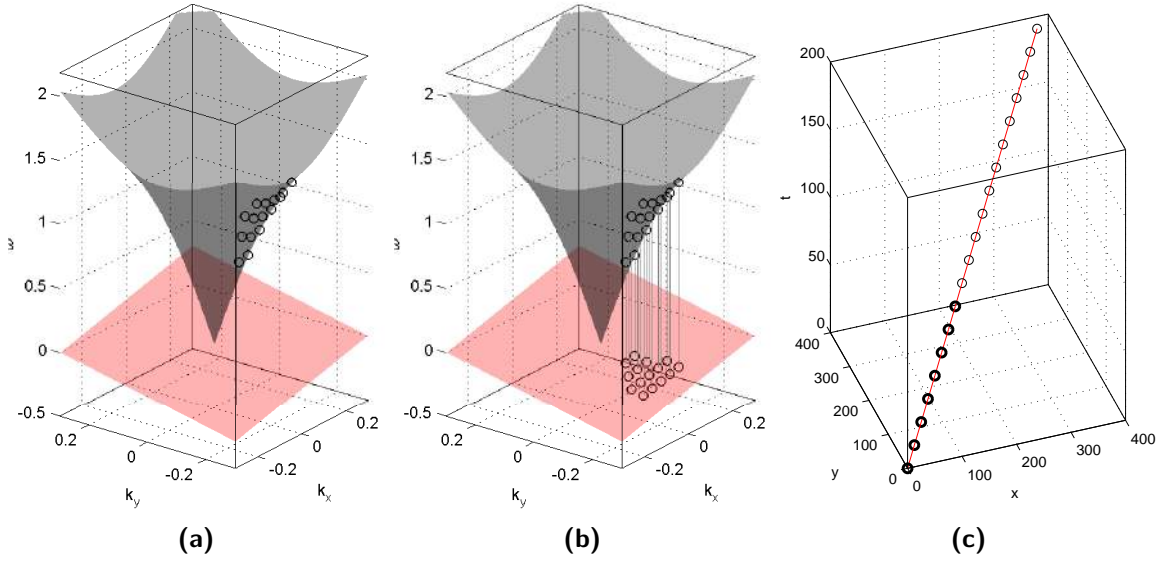


Figure 3-7: Figure a shows in black the complete dispersion shell for $d = 7$ meter, $U_x = 0.5$ [m/s] and $U_y = 0.5$ [m/s]. In red the dispersion shell compensated for the depth term is plotted, which result in a plane. The black circles are the spectral data points used for illustration. Figure b shows the result of the depth compensation which moves the spectral data to the plane. Figure c shows the result after the transformation back to x, y, t -space with an IFFT. These bold printed circles are used to fit the line which results in a current estimate.

are used for illustration.

The contributions of the energy density spectrum will lie on a plane if the depth is estimated correctly, which is shown in Figure 3-7b. The compensated spectrum is then transformed back to the x, y, t domain with a 3D IFFT. For a perfect plane this transformation results in the following set of equations:

$$\begin{aligned} x &= U_x t \\ y &= U_y t \end{aligned} \quad (3-9)$$

Figure 3-7c shows the points in x, y, t -space after the transformation. The points lie exact on the searched line in this example, which is the result of the "perfect" dataset chosen to illustrate this transformation. For a real spectrum like the one plotted in Figure 3-3, the points will not all lie exactly on the plane after the depth compensation, as the depth estimate will not be perfect, and the energy density spectrum will also contain contributions from other objects than waves (e.g. marker buoys). As a consequence the points in x, y, t -space will not form a perfect line.

Due to these imperfections a routine to find the optimal line fit is needed. For each t -plane the centre of gravity of the intensities in the plane is calculated. This results in 64 locations of maximum intensities. For each set of eight successive points, a line through the origin is fitted and the RMSE is calculated. The fit with the smallest RMSE is the final fit from which U_x and U_y are determined. Figure 3-8 is the final line fit of the spectrum shown in Figure 3-3

The current estimate from the first iteration is used to derive a new depth estimate. This new depth estimate is then used for a new current estimate. This iterative process is repeated 3 times before the final depth and current estimate is found. The final fit is shown in Figure 3-9

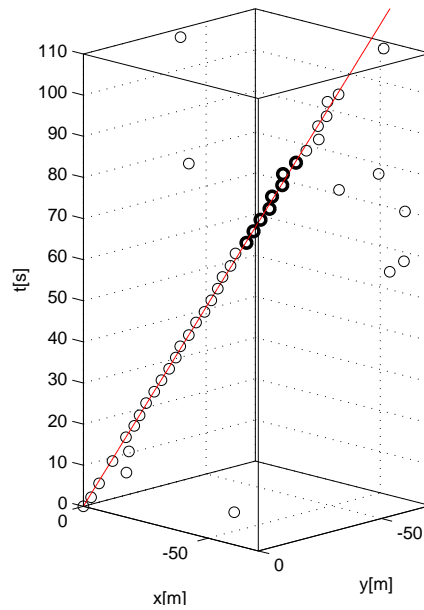


Figure 3-8: This figure is an example of a final line fit. The circles indicate the location of the maximum intensity for each t -plane. The bold printed circles are the point which are used for the line fit and red this final fit is plotted

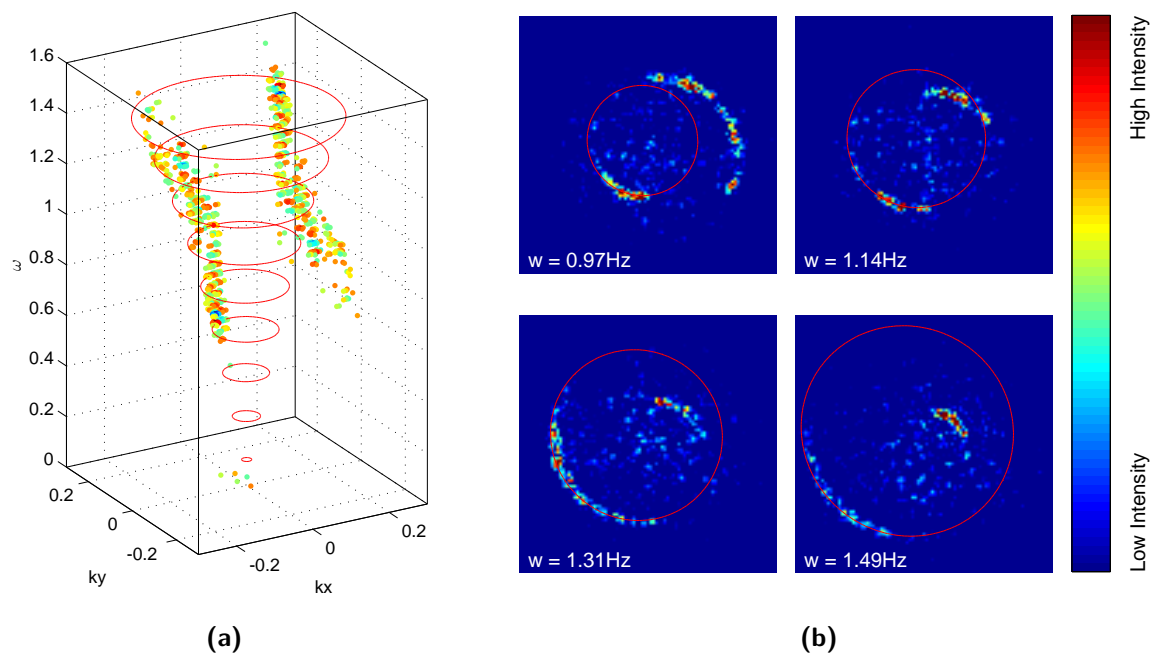


Figure 3-9: The left figure shows the final fit of the dispersion relation in red circles. From the energy density spectrum only the high intensity contributions are plotted. In the left figure four omega planes are plotted together with the dispersion relation in the red.

3-1-4 Wave length and wave period estimate

For the wavelength the derived current and depth are used to generate the exact dispersion filter. The filtered spectrum is then projected to the $k_x - k_y$ space. The energy peak gives the wavelength. After this computation, the dispersion relation is used to calculate the

corresponding wave period.

Chapter 4

Discussion

This chapter will give a critical look on the algorithm and mark the knowledge gaps which are still present. Based on this discussion chapter a number of hypotheses will be formulated concerning the limitations of SeaDarQ. These hypotheses will be used for validation in the next chapter.

4-1 Input

The SeaDarQ algorithm starts with a computational cube which is built from radar images (Chapter 3). The size of this cube and the resolution of the images determines the domain and resolution in k_x, k_y, ω -space. The maximum angular wave number (k_{max}) and maximum angular wave frequency (ω_{max}) depend on the pixel size (P) and the sampling interval (Δt), according to the Nyquist limit,

$$\begin{aligned}k_{max} &= \frac{2\pi}{P} \\ \omega_{max} &= \frac{2\pi}{\Delta t}\end{aligned}\tag{4-1}$$

Vice versa, the resolutions in wavenumber and frequency space, Δk and $\Delta \omega$, respectively, are defined from the length in space and time, expressed in terms of the number of spatial pixels (N_i), and the number of time frames (N_t), as

$$\begin{aligned}\Delta k &= \frac{2\pi/P}{N_i} \\ \Delta \omega &= \frac{2\pi/\Delta t}{N_t}\end{aligned}\tag{4-2}$$

The resolution of the images and consequently the spatial Nyquist frequencies are fixed and depend on the radar installation, but the size of the computational cube can be varied. Three aspects are important regarding the choice of the computational cube size.

The resolution of the image spectrum, which is obtained after the 3D Fast Fourier Transformation (FFT), increases with an increasing computational cube size. The lowest possible frequencies, which can be solved, also increases with an increasing computational cube size.

The second aspect is the assumptions that the conditions captured in the computational cube are homogeneous. This means that all the waves in the images should be influenced by the same depth and current for the contributions in the image spectrum to concentrate on one dispersion shell. This requirement is in conflict with the first requirement.

The final aspect regards the computational time which increases for an increasing computation cube size. When the algorithm is running live, the computational time determines the temporal resolution of the output signal.

A balance between those aspects should be made, which depends on the local hydrodynamics. For a dynamic environment in which the current magnitude and direction changes fast and a steep slope in the bottom is present, a smaller cube would be optimal than for a deep water situation with a tide driven current. No guidelines are available regarding this aspect. In Figure 4-1 an example of two image spectra for different input cube sizes is plotted. The computational for the left figure is half the size of the cube that is used for the right figure. These figures show that the contributions in the energy density spectrum concentrate better on the dispersion shell for a larger computational cube size.

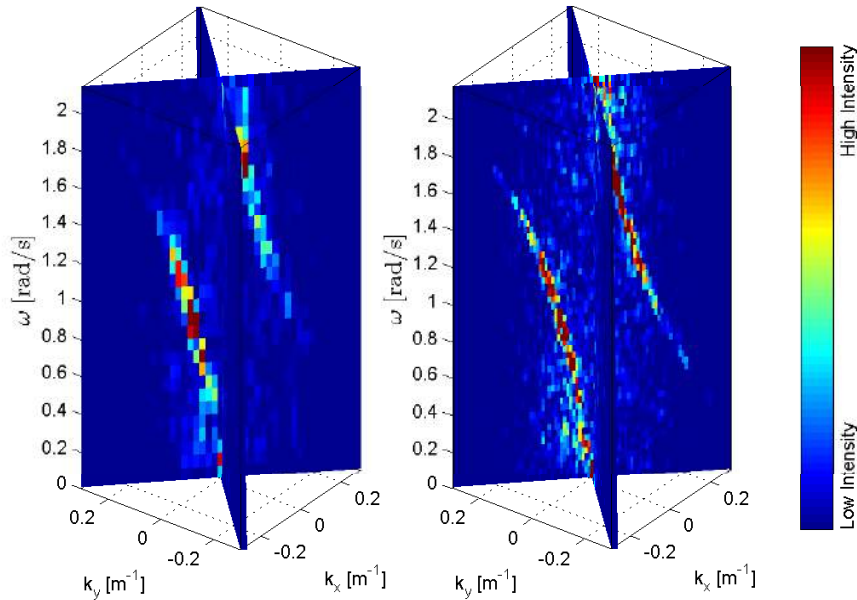


Figure 4-1: The left picture is a image spectrum for a input cube of 128x128 pixels \times 32 time frames. The right picture is a image spectrum for a input cube of 256x256 pixels \times 64 time frames. The contribution in the picture with larger domain in x, y, t and consequently a higher resolution in k_x, k_y, ω shows a better coverage of the dispersion shell and the contributions concentrate more on the dispersion shell. It depends on the hydrodynamics conditions if it is possible to use the large computational cube, since the contributions within this cube should be homogeneous.

Hypothesis 4.1. *Selecting the computational cube size based on expected hydrodynamic conditions and bottom topography improves the accuracy of the SeaDarQ output.*

4-2 Image spectrum

The spectral cube which is obtained in the end of the preprocessing phase (chapter 3) does not only contain contribution on the searched dispersion shell but also noise which can be

related to either inhomogeneities, reflections or aliasing each of which is discussed in detail below.

inhomogeneous conditions The conditions within the computational cube should be homogeneous for the contributions in the image spectrum to lie on one dispersion shell. Deviations in the conditions will spread the contributions in the image spectrum around the dispersion shell. Inhomogeneities can have both spatial and temporal causes. Variations in time can be the result of a change in current magnitude or current direction. Spatial variations can be the result of a slope in the bottom or change in current magnitude or direction due to a complex hydrodynamic structure like an eddy.

Hypothesis 4.2. *The SeaDarQ algorithm does not converge if the conditions in the computational cube are inhomogeneous, resulting in inaccurate output.*

reflections Reflections from other objects than waves have a detrimental effect on the image quality. In the preprocessing phase the influence of reflections from objects like vessels and marker buoys is filtered out mostly, but some of the reflections from these objects will remain in the images. These reflections will result in noise in the image spectrum. The clear white spots in Figure 4-2 are an example of reflections from marker buoys.

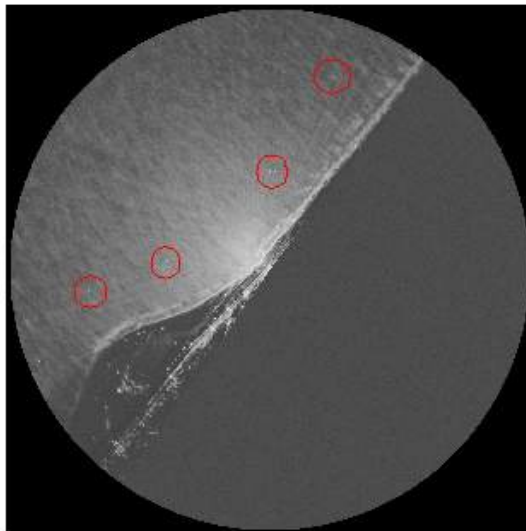


Figure 4-2: This image is a 1 minute average image of the radar reflections. The clear white spots in the image are reflections from the marker buoys around the Sand Motor.

Aliasing The limited resolution in time and space introduces aliased components (Section 3-1-2). Most of these artificial contributions are filtered from the spectrum, but there will be some remaining components which do not concentrate on the theoretical dispersion shell.

Limited resolution The linear dispersion relation will not fit exactly through the grid points of the image spectrum. As a consequence the contributions of the linear dispersion relation will

spread over the closest grid-points. One slice at $k_y = 0$ of the deep water relation ($\omega = \sqrt{g|\vec{k}|}$) is plotted in Figure 4-3 in black. The grid illustrates the sizes of the grid cells which is for illustration purposes quite coarse. The dispersion relation does not fit exactly on the grid-cell and as a consequence the contributions of the dispersion relation will spread over the closest grid-cells as illustrated in red.

Hypothesis 4.3. *The accuracy of the SeaDarQ output is correlated to the resolution of the energy density spectrum.*

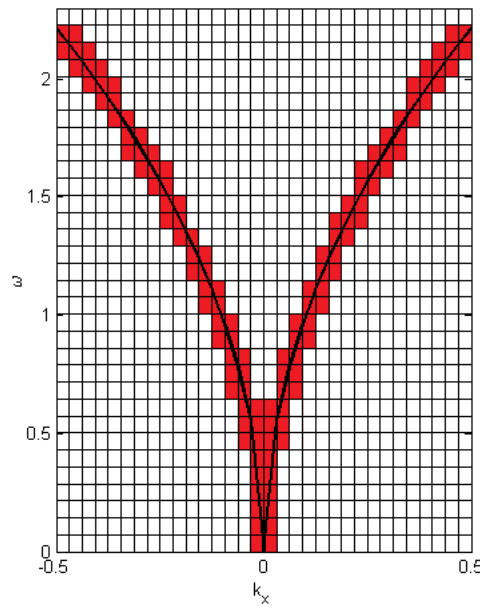


Figure 4-3: In black the linear dispersion relation is plotted. The resolution of the spectral domain is not infinite. The contributions of the linear dispersion relation will spread around the exact dispersion relation as a consequence. This is illustrated in red.

4-3 Depth and Current estimate

The depth and current are derived in a iterative fashion from the contributions in the energy density spectrum (Section 3-1-3). For the depth and current estimate a wide dispersion filter is used that is built from the dispersion relation with an lower and upper limit for the depth and the current. Those boundaries are chosen at the lower and upper limit of SeaDarQ. Research from Nortek (from which no justification is available), revealed that SeaDarQ cannot estimate depths below 5 meter and currents of more than 2 m/s. The upper limit of the depth represents deep water conditions and can be interpreted as an infinite depth. Optimizing those boundaries might improve the performance of the algorithm. For instance, when available, estimates of the bathymetry and hydrodynamics can be used to provide more realistic boundaries to improve convergence of the algorithm.

Another important aspect is the coverage of the dispersion shell. If only one wave component is available in the images, this results in one point on the dispersion shell. The number of solutions for the depth and current would be infinite. At least three contributions are needed to fit an unique solutions of the dispersion relation. At least one of the points

should lie within the frequency band of waves which are influenced by the depth. The wave direction of the other two contributions should be different. Three points which meet these requirements is enough to solve the three unknowns in the linear dispersion relation. It is, for instance, not possible to solve the linear dispersion relation for a uni-directional wave field.

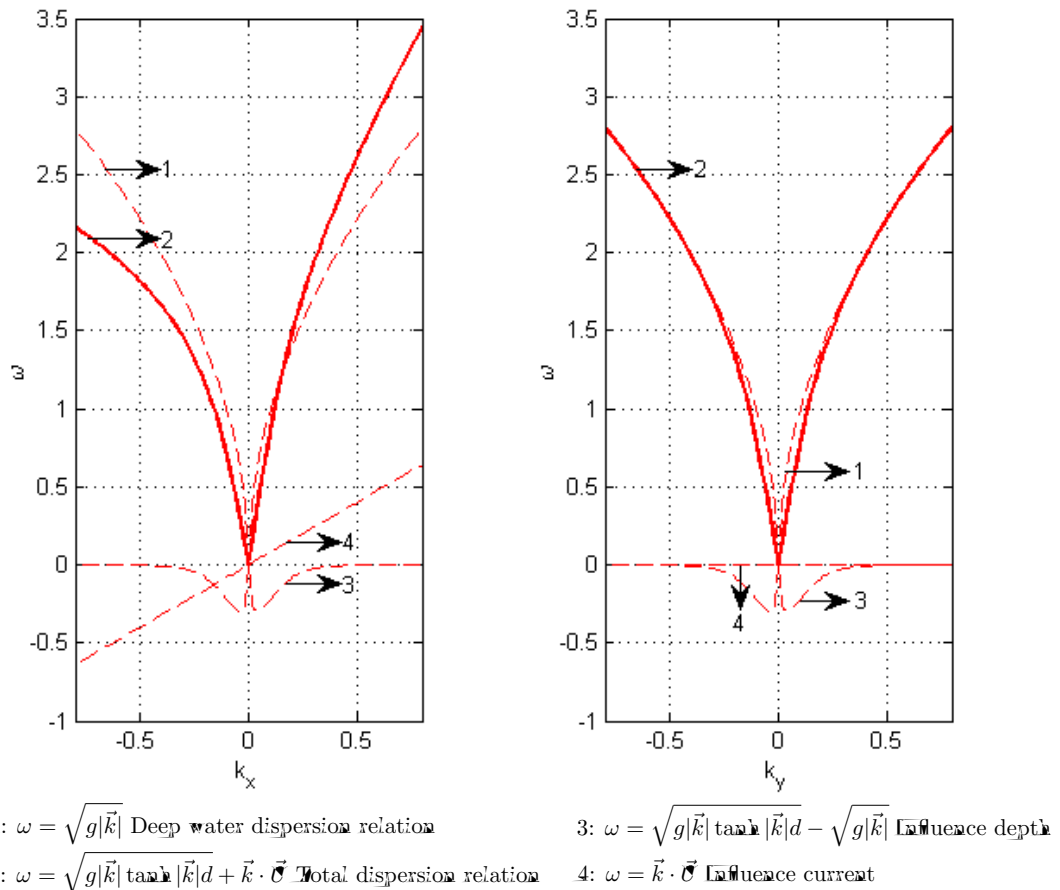


Figure 4-4: These plots show the dispersion relation and the influences of the depth and current on the shape of the dispersion shell. The left figure is a slice plot at $k_y = 0$ and the right figure is a slice plot at $k_x = 0$.

How the depth and the current influence the shape of the dispersion curve is important to understand the relation between the accuracy of the fitted current en depth by SeaDarQ. Figure 4-4 shows the dispersion shell decomposed in: the deep water relation, the depth influence and the current influence.

The water depth determines which wavenumber band is influenced by the depth. This can be expressed with the parameter $|\vec{k}|d$. The influence of the depth becomes marginal for $|\vec{k}|d > 2.3$. For a depth of 7 meter this corresponds to a wavelength of approximately 20 meters.

The deformation of the dispersion shell due to a current, increases with an increasing wavenumber. The dispersion shell bends due to the current and becomes a-symmetric about the ω -ax. The influence of the current is largest for waves which travel at the same or opposite direction as the current (Figure 4-4 left). Waves which travel perpendicular to the current are not

influenced by the current at all (Figure 4-4 right).

depth estimate To estimate the depth, it is important that the estimated current in both x and y direction is good. A small error in the current estimate influences the depth estimate significantly for kd values close to 2.3. The influence of the depth is much smaller than the influence of the current. The depth estimate becomes very sensitive in this case which is clarified with the example below.

Example 1: Sensitivity depth estimate

Depth = 10 meter

$U_x, U_y = 1, 0$ m/s

$k_x, k_y, \omega = [0.2, 0, 0.0113]$ (This is an existing point on the dispersion shell)

If a current estimate is available the depth is the only unknown which can be solved. For a current estimate which is exactly right this results in a depth of 10 meters. When the current estimate is not exactly right, but $[U_x, U_y] = [1.05, 0]$ the depth estimate becomes 7.48 meters.

A 5 percent deviation in the current estimate results in a 25 percent deviation in the depth estimate in this case.

The example above is an extreme case. For lower kd values the depth is more significant compared to the current which makes it less sensitive. The example does show that for certain wave conditions the depth estimate is very sensitive to the current estimate. In reality it is more complex, because the image spectrum contains more than one contribution on the dispersion shell. The kd values of the available contributions determines if it is possible to estimate the depth ($kd < 2.3$ should be available) and how sensitive the estimate is to the accuracy of the current estimate.

Hypothesis 4.4. *A good current estimate and sufficient wave information in the region $kd < 2.3$ is required for a good depth estimate.*

current estimate For the current estimate a good depth estimate is not necessary if $kd > 2.3$ since these waves are not affected by the depth at all. Using these waves for the current estimate will always result in the same current estimate, regardless the accuracy of the depth estimate.

The current estimate is most sensitive to the depth estimate for a small wavenumber. The smallest wavenumber depends on the computational size. For a cube of 1000 x 1000 meter the smallest wavenumber = 0.0065 (4-2). Example 2 clarifies the sensitivity of the current estimate. For this example the worst case scenario is investigated by using $k = 0.0065$.

Example 2: Sensitivity current estimate

Depth = 10 meter

$U_x, U_y = 1, 0$ m/s

$k_x, k_y, \omega = [0.0065, 0, 0.0708]$ (This is an existing point on the dispersion shell)

If a current estimate is available the depth is the only unknown which can be solved. For a current estimate which is exactly right this results in a depth of 10 meters. When the depth estimate is not exactly right, but $d = 10.5m$, the current estimate becomes $[U_x, U_y] = [0.75, 0]$.

A 5 percent deviation in the depth estimate results in a 25 percent deviation in the current estimate in this case.

The long waves are not used for the current estimate. This is a consequence of the line fitting procedure used for the current estimate. This will be explained in the next section. This will clarify why the current estimate is less sensitive to the estimated depth than this example suggests.

The current estimate also depends on the difference in wave and current direction. Waves traveling perpendicular to current are not affected by the current, and consequently they provide no information on the magnitude of the current. Fortunately, realistic wave fields are usually not uni-directional, but instead contain components traveling in directions spread around the mean direction. Although some waves will still be perpendicular to the current, usually sufficient components that travel at an acute angle with the current remain to obtain an estimate thereof. It is therefore not expected to be of major concern in most cases.

Three and a half iterations are used in the algorithm to derive the current and depth, which is a fixed number (Section 3-1-3). Research from Nortek revealed that the solution does not change after three iterations. No report of this research is available. It is not known for which conditions this is tested and if this is valid for a wide range of conditions.

4-4 Line Fit

The current is fitted in x, y, t -space (Section 3-1-3). The consequence of the fitting procedure is discussed in the section. First the orbital motion in the water due to waves is explained. This theory is used to elaborate on the valid depth for the fitted current.

The orbital motion in the water due to waves can be described with linear wave theory. Figure 4-5a is an image from (Holthuijsen, 2007) that shows this orbital movement under a wave, derived from linear wave theory. The velocities are largest at the water surface and decays towards the bottom. It depends on the $|\vec{k}|d$ factor how vast the orbital movement decays towards the bottom. Figure 4-5b shows the velocity over the depth for different wave numbers. A long wave is present over a larger part of the water column than a short wave.

The linear dispersion relation, which is used in the algorithm, assumes a uniform velocity profile over depth. However, if a vertical shear is present, the effective mean current as experienced by a wave might depend on the frequency of the wave since the short waves are only active in the top part of the water column. Consequently, the mean current that is obtained from the algorithm depends on the frequencies of the waves used to fit the dispersion shell.

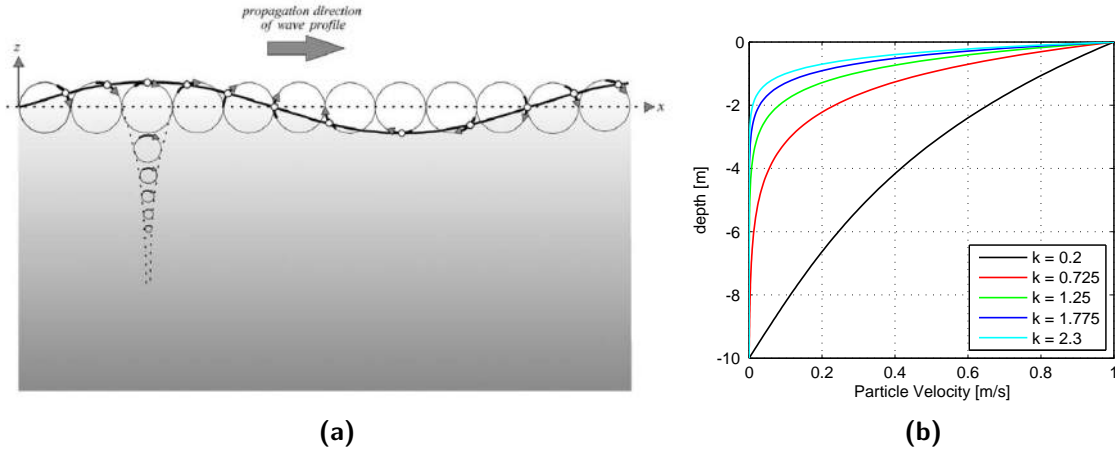


Figure 4-5: Waves induce an orbital movement in the water column. This is illustrated in the left figure. This movement decays toward the bottom depending on $|k|d$ factor. This is shown in the right figure

Within the SeaDarQ algorithm, the dispersion relation is not directly fitted to the observed frequencies. Instead, an Inverse Fourier transform is performed and the fit is performed within x, y, t space. Consequently, it is not straightforward to determine what the effective spectral range is that most strongly determines the fit of the dispersion relation, since the contributions in x, y, t -space do not relate to one specific wavenumber.

The fitting procedure in x, y, t -space can be used to determine the longest wave that is used in the current fit. The line fit does not use all the contributions available in x, y, t -space, but instead it uses 8 time-planes (Section 3-1-3). The length of the domain used in x, y, t -space corresponds to the resolution in k_x, k_y, ω -space (Section 4-1). The longest wave that is visible in the spectrum corresponds to Δk (4-2). Selecting only as small box from x, y, t -space to fit the current corresponds to increasing the Δk .

The domain used for SeaDarQ is 1000m x 1000m x 192 s. The resolution in these directions is 3.9m x 3.9m x 3s. The resolution $\Delta k, \Delta \omega$ can be calculated from these numbers,

$$\Delta k = \frac{2\pi}{1000} = 0.0063$$

$$\Delta \omega = \frac{2\pi}{192} = 0.0327$$

For the line fit eight time planes are used which corresponds to $3 * 8 = 24$ seconds. The length in x and y direction depends on the current magnitude in both directions. The new resolution can be calculated with the following equations in which N is the number of points used for the line fit:

$$\Delta k_{new,i} = \frac{2\pi}{N \Delta t U_i} \quad \text{for } i = x, y$$

$$\Delta \omega_{new} = \frac{2\pi}{N \Delta t}$$
(4-3)

Example 3 clarifies the consequence of the fitting procedure for the maximum wave length used to fit the current.

Example 3: Influence fitting procedure

$$U_x, U_y = 1, 0 \text{ m/s}$$

Domain $x, y, t = 1000 \text{ m.r} \times 1000 \text{ m.x} \times 192 \text{ sec.}$

The problem reduces to a 2D problem by assuming no current in the y direction.

The original Δk can be calculated with equation 4-2. $\Delta k_x = \frac{2\pi}{1000} = 0.0063$.

The domain in x, t direction reduced in the line fitting procedure. 8 time planes correspond to 24 seconds. The length in x -direction becomes $24 \text{ sec} * 1 \text{ m/s} = 24$ meter. $\Delta k_{new,x}$ can be calculated with equation (4-3). $\Delta k_{new,x} = \frac{2\pi}{24} = 0.2618$

The minimum wavenumber used for the current fitting is smaller for a strong current than for a weak current. This suggests that a strong current is valid over a larger depth than a weak current. The following two hypotheses can be formulated based on the knowledge about the current fitting procedure from SeaDarQ.

Hypothesis 4.5. *The longest wave contributions in the energy density spectrum are excluded from the current fit.*

Hypothesis 4.6. *The valid depth of the estimated current depends on the absolute current velocity.*

The exclusions of the long waves from the current fit affect also the sensitivity to the accuracy of the estimated depth. Example 2 shows the influence of the accuracy of the estimated depth on the current estimate. For that example the worst case scenario was used, by exploring the influence of the estimated depth on the current accuracy for the longest possible wave available in the spectrum. The current fitting procedure filters part of the long waves. The new longest waves, resulting in the new worst case scenario, can be calculated with equation (4-3). Example 4 is an example for the same condition as used in Example 2, but now with the new longest wave that is calculated in ??.

Example 4: Influence fitting procedure

Depth = 10 meter

$$U_x, U_y = 1, 0 \text{ m/s}$$

$$k_x, k_y, \omega = [0.26180, 0.4173] \text{ (This is an existing point on the dispersion shell)}$$

If a current estimate is available the depth is the only unknown which can be solved. For a current estimate which is exactly right this results in a depth of 10 meters. When the depth estimate is not exactly right, but $d = 10.5 \text{ m}$. the current estimate becomes $[U_x, U_y] = [0.9986, 0]$.

A 5 percent deviation in the depth estimate results in a 0.14 percent deviation in the current estimate in this case.

Excluding the long waves from the current fit results, for the case described in Example 2 and Example 4, in a current estimate that is insensitive to the depth estimate.

Hypothesis 4.7. *The current estimate is rather insensitive for the accuracy of the depth estimate due to the current fitting procedure.*

SeaDarQ searches for the eight consecutive points with the smallest Root Mean Square Error. These points are used for the line fitting. It is not known what the physical difference is between a fit on the first 8 time-planes or another set of 8 time-planes. More research is needed to fully understand the line fitting procedure and its consequences for the physical meaning of the fitted current.

4-5 Influence ambient conditions

The ambient conditions are important for the quality of the radar images and the wave information captured in these images. In this section the expected influences of the ambient conditions on the SeaDarQ output is discussed. The following ambient conditions are considered: wind speed, wind direction, rain, wave height, wave spreading and wave direction.

The radar signal backscatters on the capillary wind waves (section 2-1). Below a certain wind speed no capillary waves exists. In literature (Swinkels et al., 2012) 2 m/s wind speed is mentioned as the lower limit needed to get sufficient reflection. The differences in backscatter intensities determine whether waves are visible in the images or not. The standard deviation of the backscatter intensities is therefor used as a measure for the quality of the images. Images with a standard deviation lower than 0.3 are rejected and not used as input for the SeaDarQ algorithm.

Hypothesis 4.8. *The standard deviation of the backscatter intensities during wind speed lower than 2 m/s is less than 0.3 and no output will be available from SeaDarQ.*

The wind direction has a similar effect on the radar images as the wind speed. The reflection properties of the sea surface is best for wind blowing towards the radar and poorest for wind blowing in opposite direction (section 2-1). Poor reflection properties result in small intensity differences in the radar images and waves are not visible in the images in this case.

Hypothesis 4.9. *The standard deviation of the backscatter intensities for wind blowing over the radar towards the sea, or close to this direction, is less than 0.3 and no output will be available from SeaDarQ.*

Another ambient condition that influences the backscatter properties of the water surface is rain. When a rain drop hits the water surface a small wave is created with similar dimension as the small capillary wind waves. The radar signal reflects also on the waves originating from the rain drops. The reflection properties of the water surface are similar over the complete area during heavy rain. The intensity differences are small in this case and no waves can be distinguished in the radar images.

Hypothesis 4.10. *The standard deviation of the backscatter intensities during rainy conditions is less than 0.3 and no output will be available from SeaDarQ.*

The fitting of the current and depth is based on the wave information captured in the radar images. The capillary wind waves are modulated by the long sea waves. This modulation changes the reflection properties over the long sea waves. The long sea waves are visible in the

radar images due to this differences in reflection properties (section 2-1). Besides a certain wind speed also long waves are required to capture wave information in the radar images to fit the dispersion relation through. The wave height is a measure for the availability of long waves.

Hypothesis 4.11. *A minimum wave height is required for the radar images to contain sufficient wave information to fit the linear dispersion relation.*

Directional wave spreading partly determines the coverage of the dispersion shell. The coverage of the dispersion shell is important for an accurate fit of the linear dispersion relation through the contributions in the energy density spectrum.

Hypothesis 4.12. *A minimum directional wave spreading is required to for an accurate fit of the linear dispersion shell.*

The wave direction with respect to the current direction determines whether the Doppler shift due to the current is visible in the waves. The deformation of the dispersion shell due to the depth and current is explained Section 4-3. No Doppler shift is visible in the waves that travel exactly perpendicular to the current direction. The influence of the current on the shape of the dispersion shell is minimal for waves traveling close to this condition.

Hypothesis 4.13. *Wave conditions with a small amount of spreading, traveling perpendicular to the current direction result in an inaccurate fit of the dispersion shell.*

4-6 Influence hydrodynamic conditions

The final aspect that is considered in this chapter is the validity of the linear dispersion relation. This relation, which is used to determine the depth and current, is derived from linear wave theory. The main requirement for the linear wave theory to be valid is that the amplitudes of the waves are small compared with the wave length and water depth. The second important aspect is the Doppler shift term in the linear dispersion relation that accounts for the wave current interaction. The velocity profile over the depth should be uniform for this approach to be valid.

The separation between linear and non-linear behaviour is not strict and for many non-linear situations the linear approach results still in good estimates. Non-linearities in the waves behaviour can be expressed with the kd number. This number expresses the wave length over depth ratio. This number decreases towards shallow, non-linear conditions. The uniformity of the velocity profile can be expressed in shear over the water column. The shear increases for non-uniform velocity profiles over the depth.

Hypothesis 4.14. *SeaDarQ is limited by non-linear conditions that can be expressed in a minimum kd value and maximum shear over the water column.*

Two Weeks Case Study

In the previous two chapters a description and discussion of the SeaDarQ algorithm is given. The result of this algorithm analysis is a number of hypotheses about the output and limitations of the algorithm. This chapter contains a case study to test several of the formulated hypotheses. The focus will be on the current output of the SeaDarQ algorithm. The tested hypotheses are treated in three separated groups: the first group involves the influences of the processes in the algorithm (Hypothesis 4.6 -4.7) , the second group contains the influences of the ambient conditions (Hypothesis 4.8 - 4.13) and the third group contains the hypothesis about the effect of non-linear wave conditions and non-uniform velocity profiles (Hypothesis 4.14).

The location of the case study is first introduced, followed by the measurement data available for the validation. Several comparisons between measurement data and SeaDarQ are presented next to test the hypotheses.

5-1 Sand Motor

A X-Band radar is installed at the Sand Motor and SeaDarQ software is used to estimate current, depth and wave information. The Sand Motor is a large scale nourishment along the Dutch coast at Ter Heijde. This large scale nourishment is a peninsula containing about 20 million cubic meters sand. This sand will spread due to natural forces like currents, waves and wind along the Dutch coast in 20 years. This nourishment replaces the yearly beach nourishment preventing the coast from erosion. The advantage of the large scale nourishment compared to the yearly nourishments is the smaller environmental impact. During the 20 years in which the Sand Motor will prevent the coast from erosion, no interventions are necessary which allows nature to develop. Another advantage is the recreation area it creates which is suitable for walking, surfing and beach guests.

The Sand Motor is a pilot project that is monitored to investigate if it behaves like expected and to gain more knowledge about coastal processes like sediment transport, waves and nature development. A lot of measurement data is available from the monitoring program, such as current data from an Acoustic Current Doppler Profiler (ADCP) and wave data from a wave buoy. This creates a great opportunity to validate the velocity output from SeaDarQ.

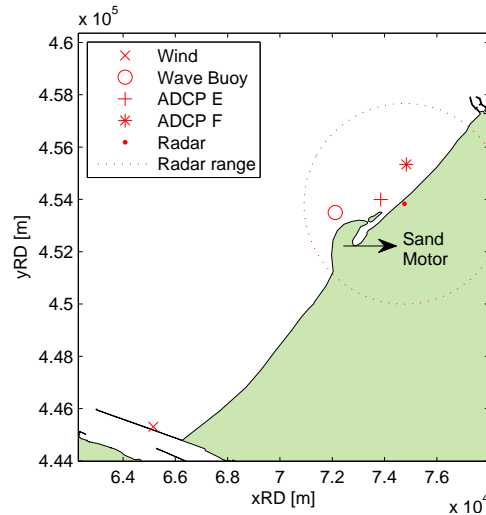


Figure 5-1: Location of the measurement devices at the Sand Motor

Therefore a X-Band radar is installed also at the Sand Motor. The locations of the different measurement devices are indicated in Figure 5-1.

The raw images from the radar are processed at the radar installation with the SeaDarQ algorithm and the output from the algorithm is stored. The raw images from the radar are overwritten in a loop of three weeks because of capacity reasons. About 2 months of raw images have been stored permanently for further analysis.

5-2 Data sets

The different measurement devices which are installed at the Sand Motor are discussed in this section. The properties of each system and an example of the output will be given for each system.

5-2-1 Marine X-Band Radar

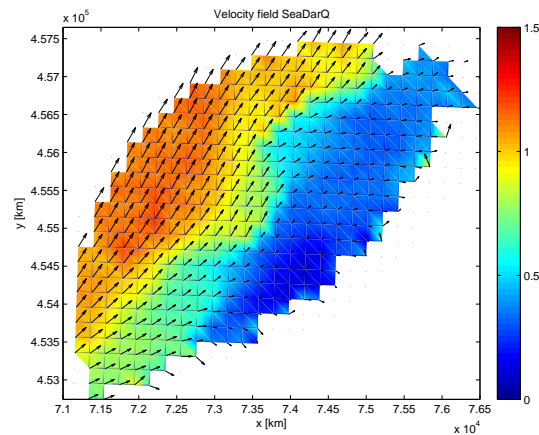
A Marine X-Band Radar is installed by Nortek at Kijkduin (Figure 5-2a). The rotation time of this radar is about 3 seconds. The raw images are only stored for a couple of weeks, because the storage capacity is not big enough to store them all. The images from the radar are processed continuously with the SeaDarQ algorithm which output is stored permanently. In Figure 5-2b an example of a velocity field estimated with SeaDarQ is plotted. The spatial resolution of the output field is approximately 200 x 200 meters and the temporal resolution is approximately 15 minutes.

5-2-2 Acoustic Doppler Current Profiler

Two ADCPs from Rijkswaterstaat are used to measure the velocity profile over the depth. The locations of ADCP-E and ADCP-F is indicated in Figure 5-1. The water depth at these locations is 6 and 9 meters. The ADCPs is mounted on a frame on the seabed and looking upwards. The frame is positioned about 1.5 meters above the seabed and measurements are



(a) X-Band Radar at Kijkduin



(b) Typical velocity field output from SeaDarQ

Figure 5-2

available from 3 meter above the seabed till 2 meter below the water surface. The raw data

**Figure 5-3: Acoustic Current Doppler Profilers**

is processed by Aquavision. The ADCP emits a signal which is reflected by particles in the water column. The Doppler shift in the received signal is used to determine the velocity. For the processing a signal of 1 minute is used and the emitted signal covers an area of approximately 1×1 meter. For the processing the water levels measured at Schevening are used with an offset in phase and amplitude. The bottom tracking signal from the ADCPs is used to determine this offset. The velocity is derived for bins of 0.5 meter and the temporal resolution is 5 minutes. In Figure 5-5 an example of the available output is plotted.

For the data analysis current information over the complete depth is needed. The measured velocities are extrapolated to obtain the complete velocity profile over the depth. The velocity near the bed is assumed to be zero and the velocity at the water surface is assumed to be the same as the velocity measured closest at the water surface. Linear interpolation between all the points is used to get a continuous velocity profile. Figure 5-4 shows the obtained velocity profile over the depth for two points in time. These figures show that this extrapolation does not always follow trend of the measured points.

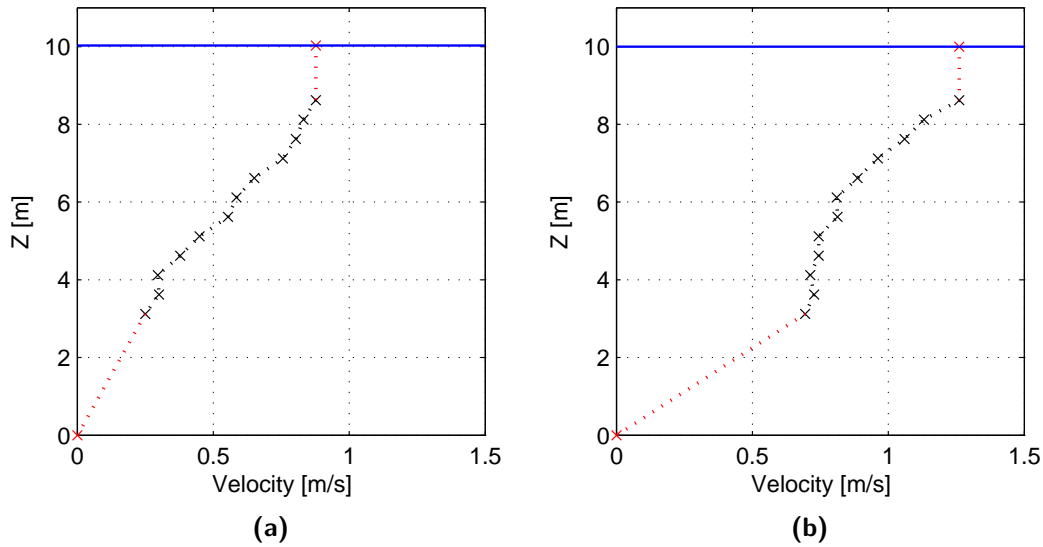


Figure 5-4: The ADCPs are not able to measure the velocities over the complete water column. The velocities near the bottom and water surface are extrapolated to fill the data gaps. This is illustrated in the figures.

For the comparisons between SeaDarQ and ADCP data different depth averages are needed. The extrapolated ADCP output is therefore averaged from the water surface till a certain distance (Δz) below the water surface. This is illustrated in Figure 5-6

5-2-3 Metocean

A Wave Buoy is deployed to measure the wave climate at the Sand Motor. The raw data from the wave buoy is processed by Rijkswaterstaat. The temporal resolution of the processed data is 20 minutes. Wind speeds and directions are measured at Hoek van Holland Noorderdam. This measurement is also done by Rijkswaterstaat. The temporal resolution of this dataset is 10 minutes. The metocean climate for the period from November the 29th till December the 10th is plotted in Figure 5-7.

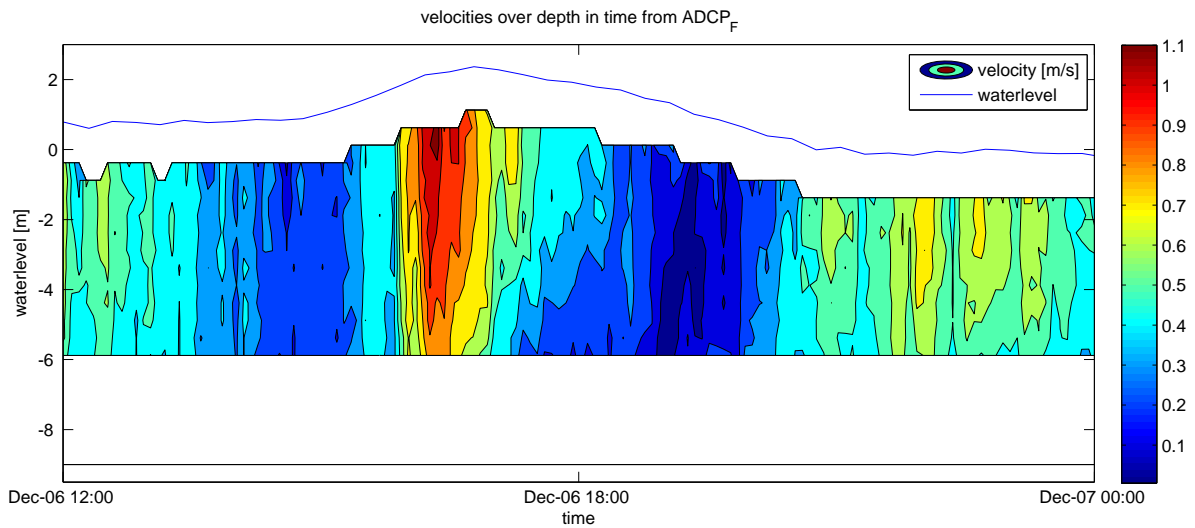


Figure 5-5: Acoustic Current Doppler Profilers contour plot. The blue line is the water level with respect to NAP and the black line is the bed level.

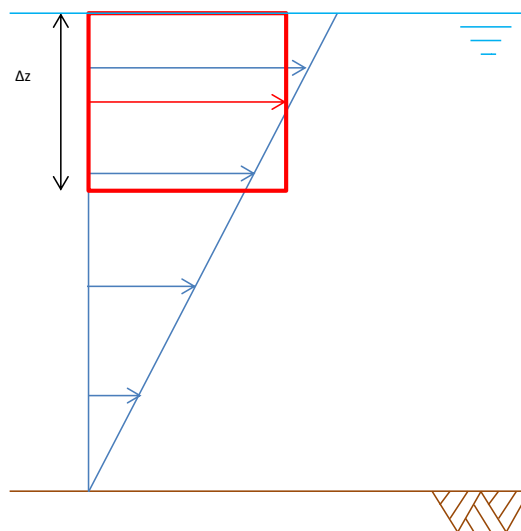


Figure 5-6: In blue a theoretical velocity profile over the depth is plotted. Δz indicates the depth over which this velocity is averaged. In red an example of an averaging is given with the resulting velocity.

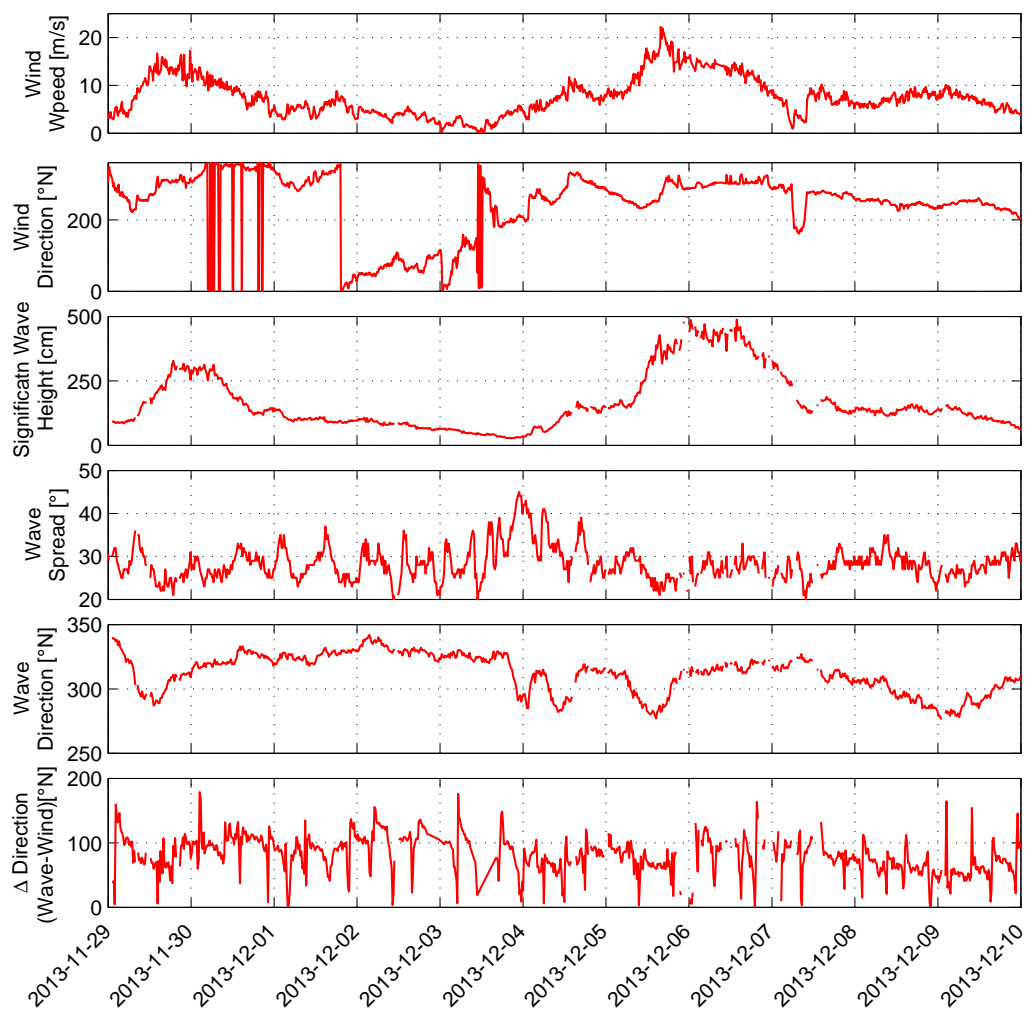


Figure 5-7: Metocean conditions measured between 29th of November and 10th of December.

5-3 Data analysis

The data analysis starts with a comparison between ADCP-F measurements and SeaDarQ current output for November 29th till December 10th to get a first estimate of the SeaDarQ current accuracy. Subsequently, other analysis are performed to test several of the hypotheses from chapter 4.

5-3-1 Comparisson between ADCP and SeaDarQ

One of the most important questions is the valid depth for the velocity output from SeaDarQ. Several studies suggest that the velocity derived from the X-Band radar images is a depth averaged surface current. The SeaDarQ output is therefor compared with different depth averaged surface velocities derived from the ADCP data (Section 5-2-2). Three different scale scores are calculated for each of the comparisons: Root Mean Square Error, Correlation and the Bias. The result is plotted in Figure 5-8. The result for the velocity magnitude is plotted in the upper panel and the result for the velocity direction is plotted in the lower panel.

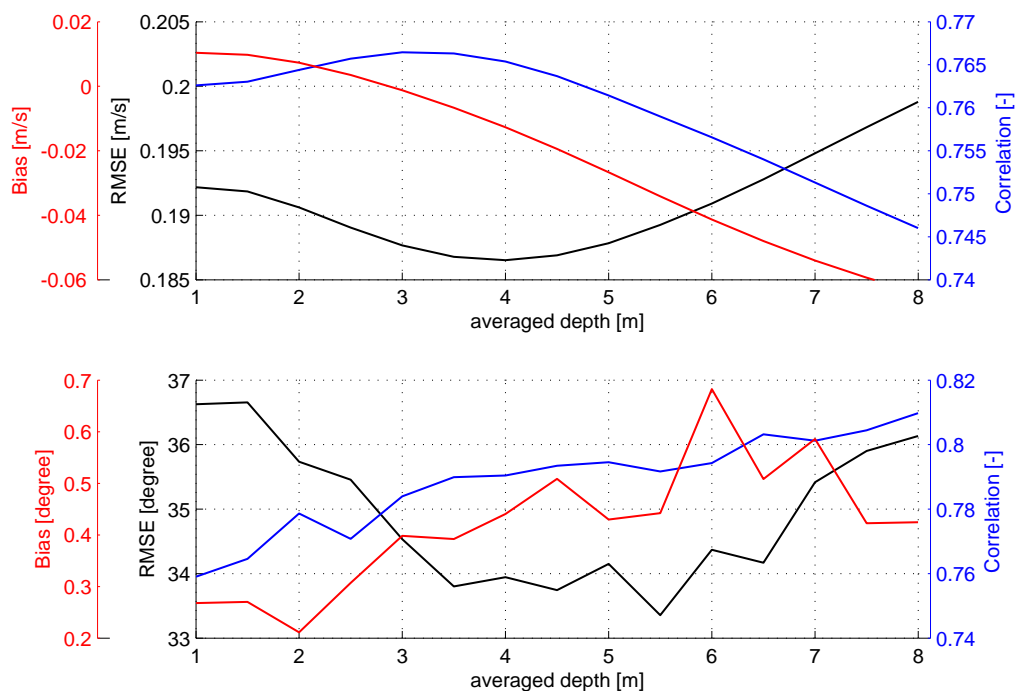


Figure 5-8: The scale scores for the comparison of SeaDarQ velocity output with different depth averaged velocities derived from the ADCP data. The upper panel contains the result for the velocity magnitude and the lower panel the result for the velocity direction.

The velocity magnitude output from SeaDarQ compares the best with the 3 to 4 meter depth averaged surface current. The scale scores for the velocity direction give a less clear best depth averaged current.

The 3.5 depth averaged surface current from the ADCP together with the SeaDarQ output and the difference of those two are plotted in Figure 5-9. The upper panel again shows the

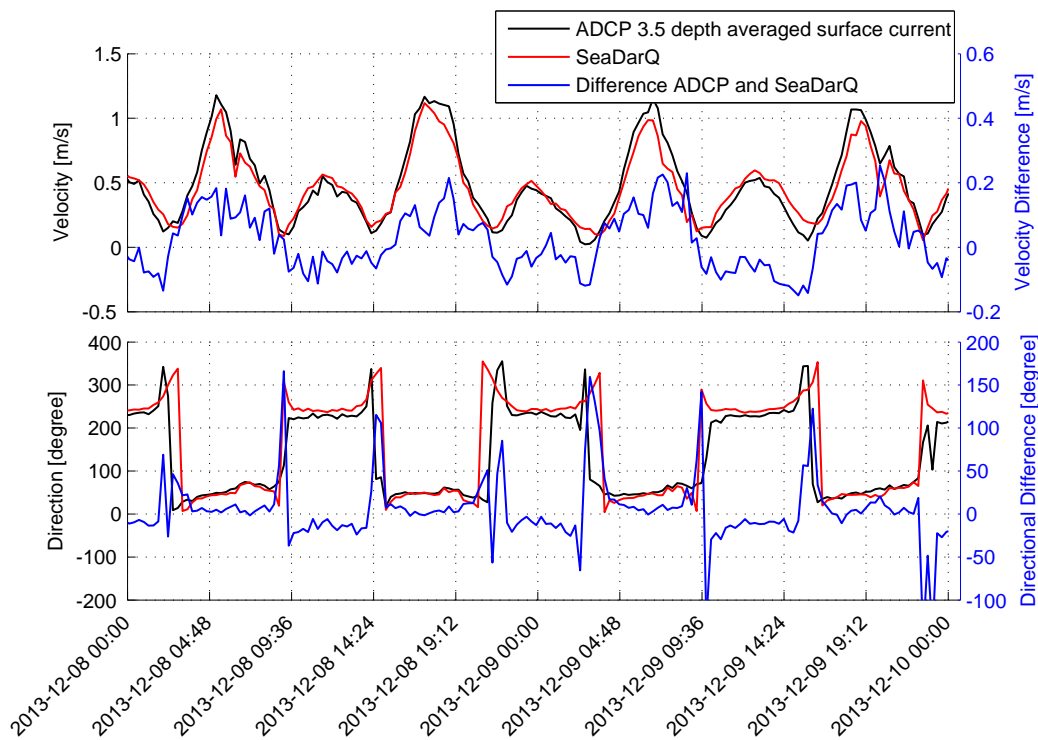


Figure 5-9: The SeaDarQ output, 3.5 meter depth averaged surface current measured with the ADCP and the difference between those two are plotted to show the comparisons between the two measurement devices.

velocity magnitude and the lower panel the velocity direction. The comparison between the two datasets is really good. It can be concluded that SeaDarQ can be used to derive current information from X-Band radar images. The RMSE for the derived velocities during the two weeks is 0.187 [m/s]. The 3.5 depth averaged surface current will be used for further analysis in this chapter.

The SeaDarQ velocity output follows the ADCP signal precisely. The distinct velocity peaks in the beginning and end of the time series are captured with both measurement systems. The tidal movement is visible as one high velocity peak, which coincides with high water, followed by a lower velocity peak, which coincides with low water. It is remarkable that the high velocity peak is always underestimated and the low velocity peak is always overestimated by SeaDarQ. This trend is best visible in the differences between both velocities. The SeaDarQ velocity direction output generally follows the ADCP measurement very well. The large outliers are found during the turning of the tide when low velocities are observed. The velocity direction is more sensitive for low velocities than for high velocities. This is illustrated in Figure 5-10. Two velocities are drawn, one large velocity in black and one small velocity in red. A disturbance of the velocity result in directional deviation that is larger for the small velocity than for the large velocity. This is probably the reason why the velocity direction output is inaccurate at low velocity conditions. Another reason can be the inhomogeneous conditions during the turning of the tide, but this is less likely since the tide is a slow movement compared to the time captured in one computational cube (Chapter3).

Similar to the velocity magnitude a correlation between the tidal movement and the difference between SeaDarQ and the ADCP data is visible for the velocity direction. The direction is always overestimated for the flood flow and underestimated for the ebb flow. This trend that

can have multiple causes:

- an incorrect alignment of the X-Band radar. The location and orientation of the X-Band is important to determine the alignment of the radar images. An offset in orientation of the radar results in a constant offset in current magnitude and direction.
- a variable valid depth in time. Hypothesis 4.6 states that the valid depth for the velocities depends on the velocity magnitude. This will be further discussed in the next section
- the ADCP extrapolation is incorrect. The ADCP measurement are vertically extended to the water surface (Section 5-2-2). This extrapolation probably underestimates the velocity near the surface especially during high velocities (Figure 5-4b)

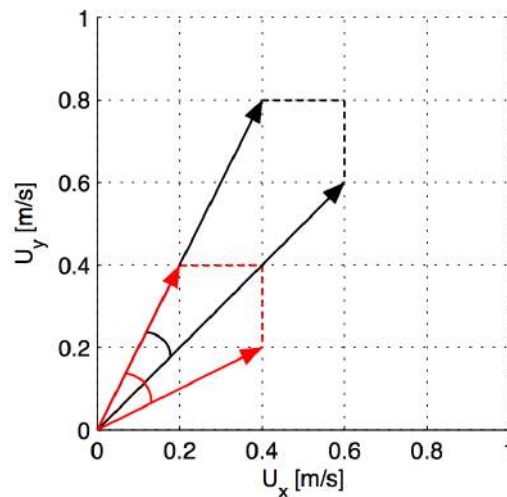


Figure 5-10: The deviation of the current direction due to an inaccurate velocity measurement in x and y direction is larger for low velocities than for high velocities. This is illustrated with a high velocity in black and a low velocity in red.

5-3-2 The influence of current fitting

Two hypotheses are stated about the validity and sensitivity of the current output from SeaDarQ (Hypotheses 4.7 and 4.6). These hypotheses are both tested in this section. Two days with rather constant metocean conditions are selected for these tests to exclude the influence of changing metocean conditions.

The first hypothesis states that the accuracy of the estimated current is rather insensitive to the accuracy of the estimated depth. This is based on the fact that the relative long waves are excluded from the current fitting. The relative long waves are most influenced by the depth. Relative short waves ($kd > 2.3$) are not influenced by the depth at all.

Two calculations with predefined depth are done to test the first hypothesis. A run with a predefined fixed depth of 9 meters and one with a fixed depth of 100 meters is performed. 9 meters water depth is rough estimate that deviates maximal 1.5 meters from the real depth. The 100 meter water depth corresponds to a deep water situation without a depth correction. The estimated depth from the original SeaDarQ run and the water depth measured at Scheveningen, with the same phase and amplitude offset as used for the processing of the

ADCP data, are plotted in Figure 5-11. The original SeaDarQ current output and ADCP current output are plotted in Figure 5-12 together with the output from the two fixed depth cases.

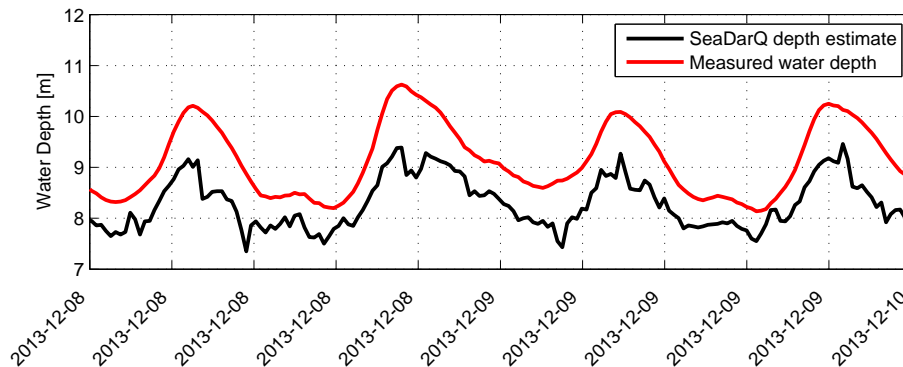


Figure 5-11: The depth measured at Scheveningen with an offset for the amplitude and the phase is plotted in red and the depth estimate from SeaDarQ in black.

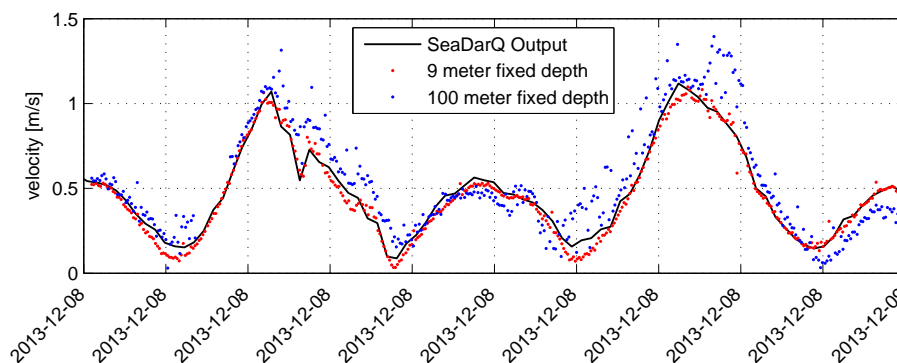


Figure 5-12: The original SeaDarQ output is plotted in black. The output from two extra runs with the depth fixed at 9 and 100 meter is plotted in red and blue.

The accuracy of the estimated current from the original and 9 meter fixed depth run are similar. The RMSE of the original run for this day is 0.088 m/s and the RMSE for the run with fixed depth at 9 meter is 0.072 m/s. So a rough depth estimate is indeed sufficient for a good current estimate. Not correcting at all for the depth results in a significantly less accurate current output as illustrated with the 100 meter fixed depth run. The wave information that is used for the current estimate is partly affected by the depth.

The second hypothesis about the current fit is that valid depth for the current differs with the current magnitude (Hypothesis 4.6). The longest wave used for the fitting of the current depends on the current magnitude. For a high velocity this wave is longer than for a low velocity. A long wave acts over a larger depth than a short wave. Consequently, the long wave is affected by the current acting over a larger depth than a short wave.

This is only important when the velocity profile is non-uniform. To investigate this hypothesis the best depth averaged surface current for every single time step is determined. Figure 5-13

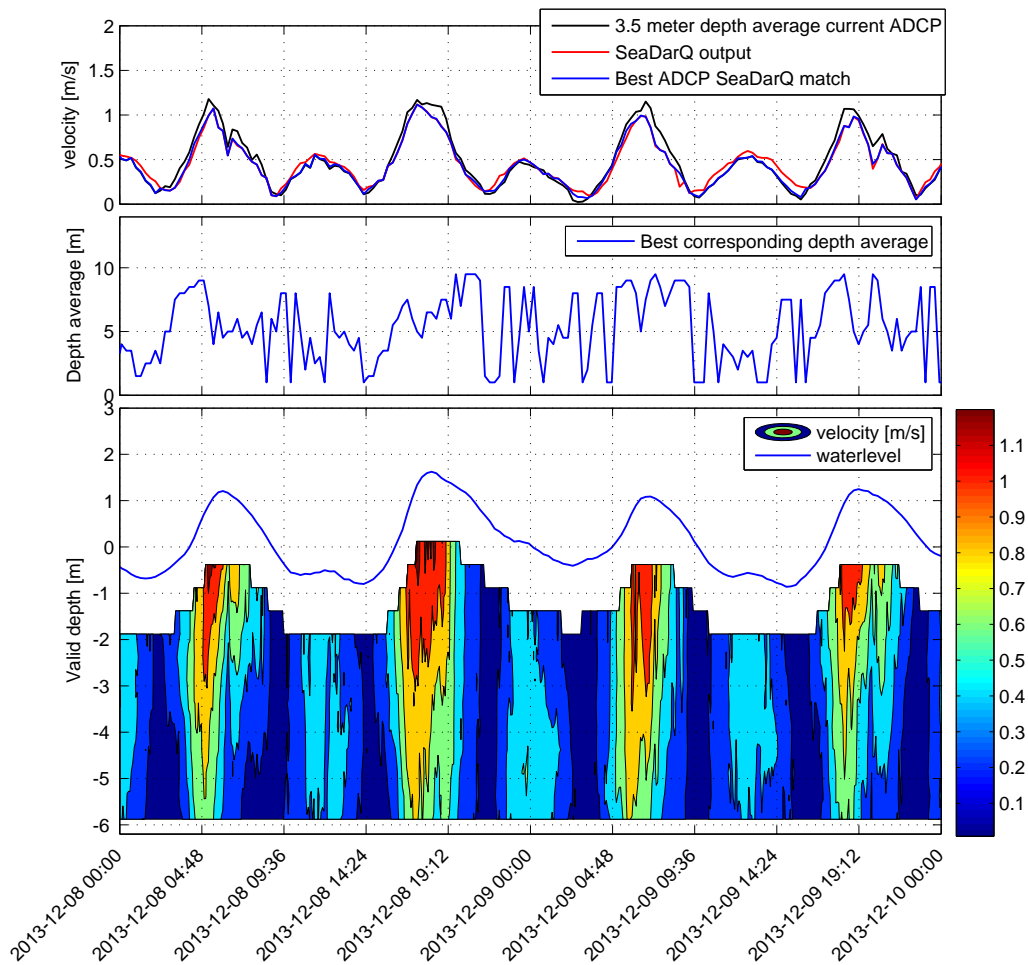


Figure 5-13: The 3.5 meter depth average velocity from the ADCP measurements and SeaDarQ output are plotted in the upper panel together with the best match between the ADCP data and SeaDarQ data. The lower panel shows the Δz used for the ADCP averaged velocity which resulted in the best match with the SeaDarQ velocity.

shows the best corresponding current in the upper panels. The second panel shows the corresponding depth for every time step and in the third panel the velocity profile over the depth is plotted. The velocity is close to uniform during ebb flow, but during flood flow significant shear in the velocity profile is measured. During these periods with significant shear no correlation between valid depth and the velocity magnitude is visible. The velocity magnitude is not the single, or most significant factor for the valid depth for the SeaDarQ output. The result is probably also influenced by the wave field that determines the coverage of the dispersion shell, the accuracy of the depth estimate and the depth itself. The depth determines which wave components are significantly influenced by the depth.

5-3-3 The influence metocean conditions

Hypothesis 4.8 states that no SeaDarQ output will be available for wind speeds lower than 2 m/s. Figure 5-14 is a time-series from wind and SeaDarQ data. The wind speed is measured at Hoek van Holland Noorderdam at 14 kilometers distance from the radar. The red thick line indicates the 2 m/s wind speed limit. During low wind speeds indeed no SeaDarQ output is available. The low quality radar images are filtered correctly by the algorithm. It is important to conclude that the algorithm does not give output instead of inaccurate data.

During the first gap in the SeaDarQ output wind speeds above the limit are observed. This is probably the result of inaccuracies in the wind data due to the distance between the measurement point of the wind and the SeaDarQ output point.

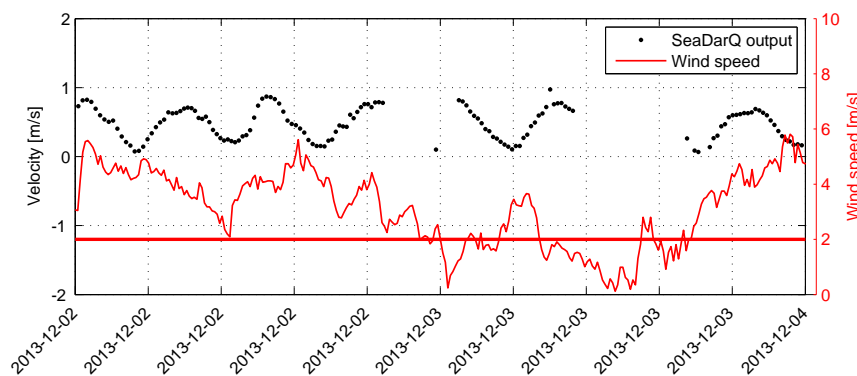


Figure 5-14: SeaDarQ output and wind speeds for a period with low wind speeds. The from literature (Swinkels et al., 2012) known minimum wind speed of 2 m/s is marked with an horizontal line. No SeaDarQ output is available during low wind speeds.

Hypothesis 4.9 states that no SeaDarQ output will be available for wind blowing over the radar towards the sea. The ADCP is located North of the X-Band radar. Wind from the South is in the worst case scenario for this location. In the metocean conditions (Figure 5-7) two short periods with wind from land are visible at December 3th and December 7th. The wind speed is for both periods above the required 2 m/s.

For both periods no change in the accuracy of the SeaDarQ output is observed. The reflection property of the water surface is still sufficient to derive accurate currents from the X-Band radar images.

Hypothesis 4.10 states that no SeaDarQ output will be available during rainy conditions due to backscatter from the waves originating from the rain drops. In the right panel of Figure 5-16 an example is given of an image in which the rain is visible as white clouds, indeed masking the waves in the image. In the left panel the output signal of the current estimate from SeaDarQ is plotted. The images are not from exact the same time since the output signal for both sources is available at same moments. The gaps in the output are probably due to the rainfall. It is important to notice that the filtering works well and SeaDarQ does not give any output instead of inaccurate output.

Hypothesis 4.11 states that a minimum wave height is required to capture sufficient wave information in the radar images to fit the linear dispersion relation. The minimum observed wave height is 28 cm. Figure 5-17 shows the wave height and SeaDarQ output during the period with low wave heights. The gap in the SeaDarQ output is related to the wind speed earlier in this chapter. After the gap even lower wave heights are observed than during the

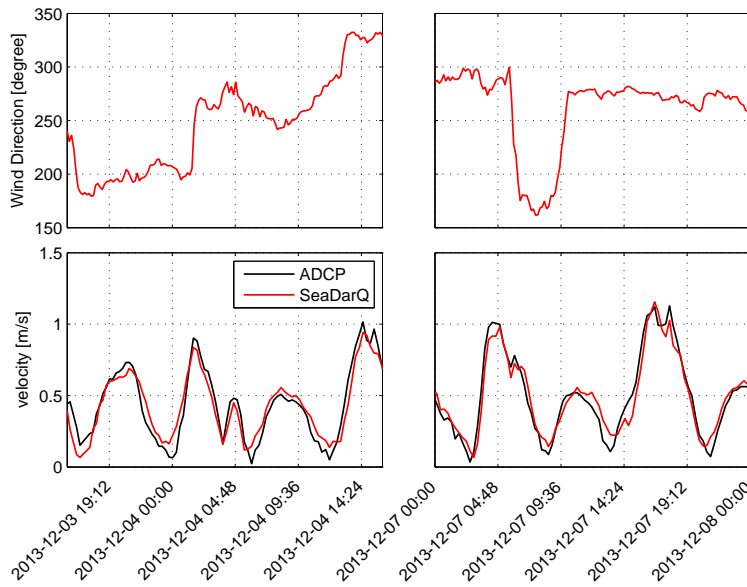


Figure 5-15: The wind direction for two periods is plotted in the upper two panels and the corresponding measured currents from the ADCP and SeaDarQ are plotted in the lower two panels. The wind direction does not influence the accuracy of the SeaDarQ output

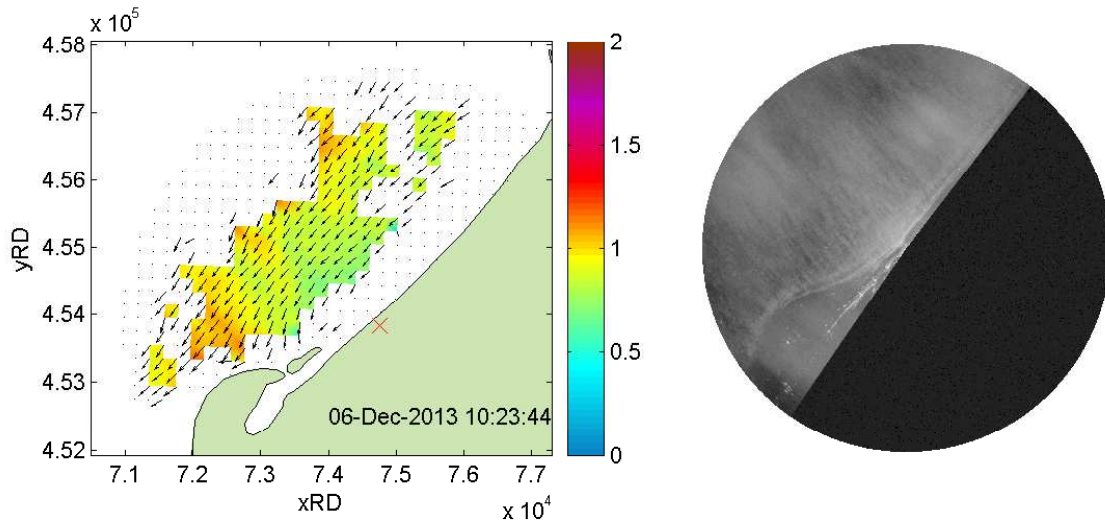


Figure 5-16: I

nfluence rain on SeaDarQ outputThe left panel shows the SeaDarQ output during rainfall. The right panel shows a 1 minute average raw image with reflection from the rainfall in the form of white clouds which mask the wave pattern.

gap and the SeaDarQ output is good, also during the minimum observed wave height. For this specific measurement location a wave height of 28 cm is sufficient to derive currents from the X-Band radar images.

Hypothesis 4.12 states that the direction waves spreading should be sufficient for an accurate fit of the linear dispersion relation. The waves spreading vary between 20 and 45 degrees during the two weeks measurement period. No correlation is found between the wave spreading

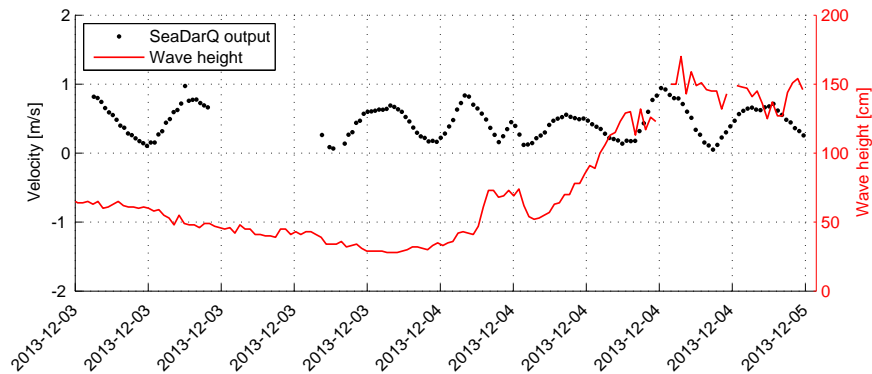


Figure 5-17: The wave height is plotted in red and the SeaDarQ output in black. During low wave height still SeaDarQ output is available.

and the accuracy of the SeaDarQ current output. 20 degrees spreading is sufficient to derive an accurate current estimate and a larger spreading does not improve accuracy of the current output from SeaDarQ. It is not possible to determine the required lower limit for the wave spreading from this dataset.

Hypothesis 4.13 states that waves traveling perpendicular to the current direction result in an inaccurate fit of the dispersion shell. The difference between wave and current direction is plotted in the lower panel from Figure 5-7. A difference of 90 degrees between current and wave direction is the most unfavourable situation to derive current from the X-Band radar. Figure 5-18 shows the difference in wave and current direction at the first day of December. This difference is in the presented period close to 90 degrees. This unfavourable condition does not affect the accuracy of the SeaDarQ output. This can be explained with the directional wave spreading that is at least 20 degrees for considered 2 weeks of data. Although the difference between wave and current direction is every tidal cycle close to 90, the current can still be estimated due to the sufficient directional spreading in the waves.

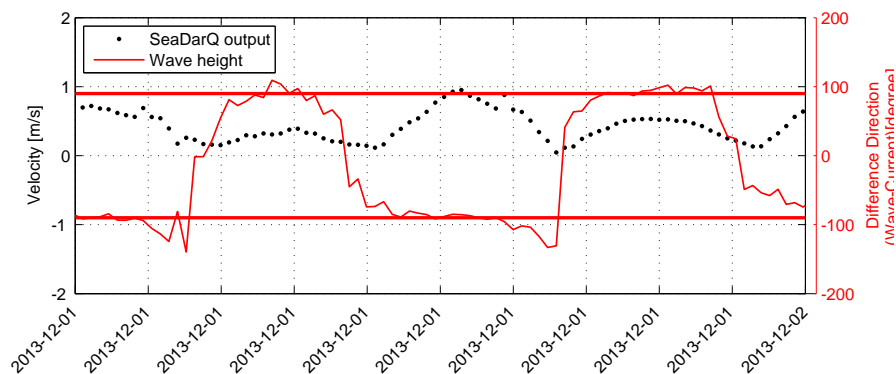


Figure 5-18: The difference between wave and current direction is plotted in red. The SeaDarQ output is plotted in black. With two horizontal lines the least favorable conditions is marked. During these conditions still SeaDarQ output is available

5-3-4 The influence non-linear conditions

Hypothesis 4.14 states that the applicability of the SeaDarQ algorithm is limited by the non-linearities in the current profile and wave behaviour. The linear dispersion relation is used to derive current and depth information from the energy density spectrum obtained with a 3D Fourier transformation from the X-Band radar images. The linear dispersion relation is derived from linear wave theory. The main restriction for the linear wave theory to apply, is a small wave amplitude and wavelength compared to the depth. The linear dispersion relation also describes the interaction between waves and a current assuming a linear velocity profile over the depth. Three different non-linear conditions are considered in this section. First the output during a non-uniform velocity profile is discussed. The second case is the output during stratified conditions and finally the output during such as storm with waves up to 5 meter is considered.

Non-uniform velocity profiles are observed every tidal cycle during maximal flood velocity (Figure 5-19). This does not affect the accuracy of the SeaDarQ output. The second considered non-linear condition is stratification. A fresh water plume is often observed near the Sand Motor (Swinkels et al., 2012). In the period from December 8th till 10th two times a fresh water plume is observed. This plume causes a sharp peak in the velocity, which is marked with two dashed ellipses in Figure 5-19. These sharp peaks are observed in both the ADCP and SeaDarQ data. SeaDarQ is also in this case able to estimate the current.

The line fit of the current is an interesting case when a fresh water plume passes by. The computational cube is large compared to the distance the density current travels in 3 minutes (approximately 100 meters). The conditions within the computational cube are not homogeneous in that case.

Figure 5-20 shows in the left panel a plot of the velocity field determined by SeaDarQ during stratified conditions. The left panel shows the raw X-Band radar image wherein the sharp line in the water represents the front of the density current. This same sharp edge is also visible in the output field from SeaDarQ. This fresh water plume also causes a jump in the velocity that is measured both with SeaDarQ and the ADCP. This jump is marked with a black dashed ellipsis in Figure 5-19. The line fit for point before and after the second jump from Figure 5-19 is plotted in Figure 5-21. The contributions in the x, y, t -domain are similar for both time steps. Two currents are visible for the two time steps which probable shows that the edge of the density current lies within the computational cube and the image spectrum also contained information for both the stratified and the non-stratified condition.

The final case is the storm conditions with high waves. In Figure 5-7 this storm is clearly visible in the wave height at December 5th till 7th. Waves of 5 meter at a water depth of 10 meter become non-linear. Waves also start to break at this depth, which is also a non-linear process. Figure 5-22 shows the ADCP and SeaDarQ output during this storm. SeaDarQ is still able to estimate the current. The Scale scores for the storm period are similar to the scale scores for the complete period of two weeks

It can be concluded that SeaDarQ can derive currents also during condition with non-linear wave behaviour and non-uniform velocity profiles over depth. This can be explained with two reasons. The first reason is the broad applicability of linear wave theory. This theory gives also a very good first estimate in non-linear situations. The second reason is the fitting procedure of SeaDarQ. For the current fit mainly short waves are used. The velocity profile is close to uniform in the upper meters of the water column where the short waves are active. The short waves are also less influenced by the bottom and become non-linear in the near-

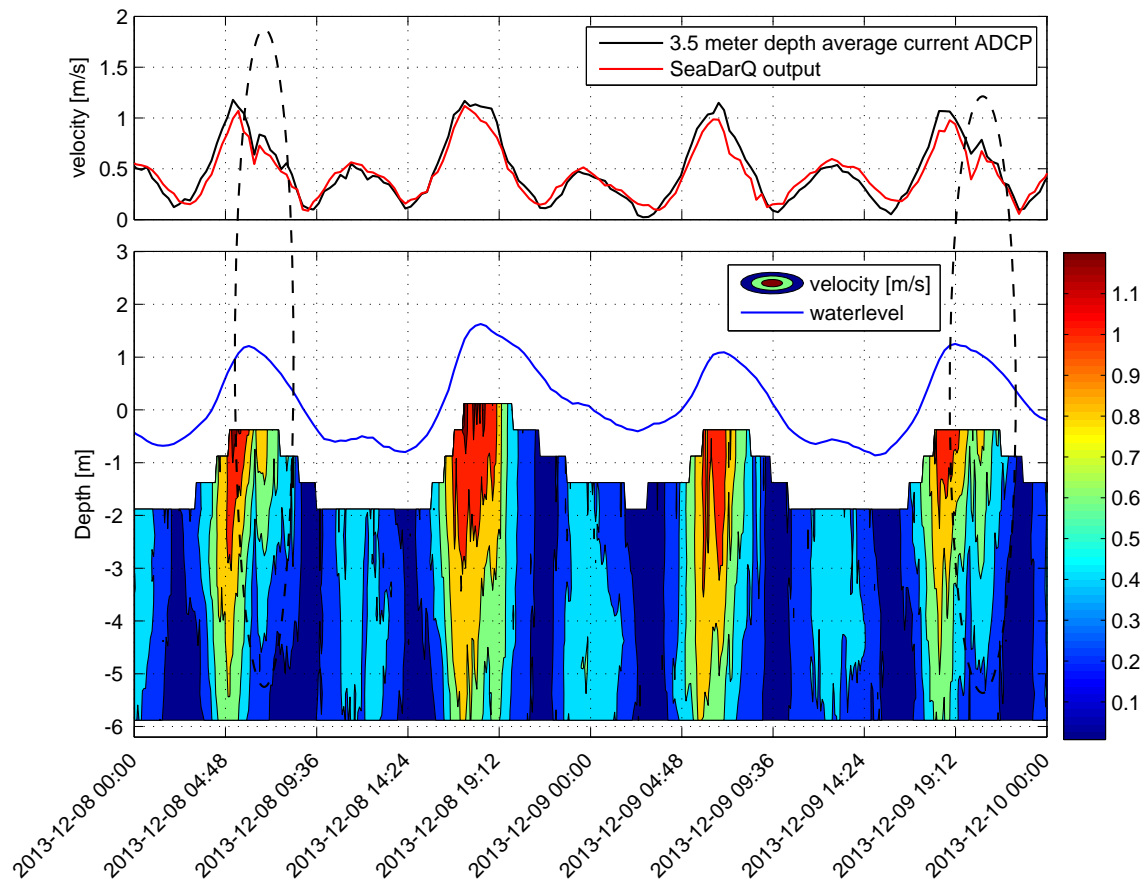


Figure 5-19: Contour plot of the absolute velocities measured with the ADCP is plotted in the lower panel. The 3.5 meter depth averaged ADCP output and SeaDarQ output is plotted in the upper panel. Two remarkable peaks in the velocity are marked with black dashed ellipses. These peaks are the result of a fresh water plume passing by.

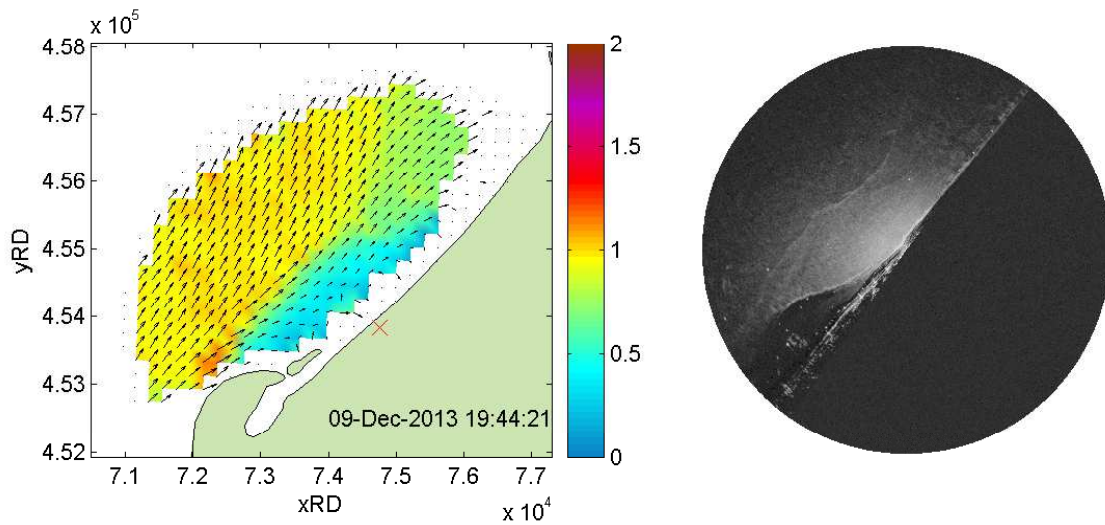


Figure 5-20: The left panel shows the SeaDarQ velocity output field during stratified conditions. In the left panel a 1 minute averaged raw radar image is plotted. The sharp line in this plot is the front of a density current.

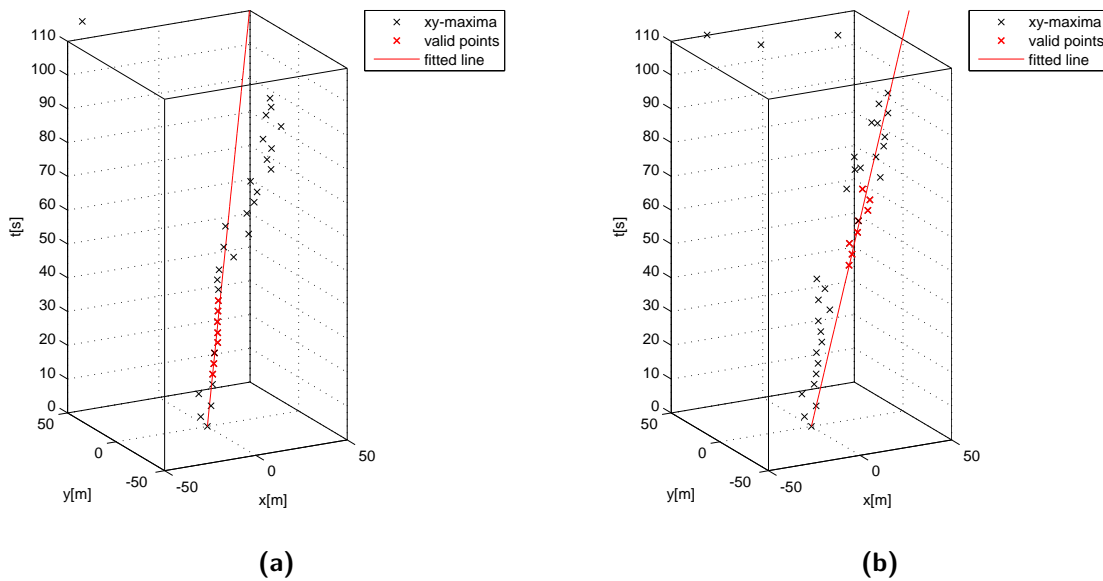


Figure 5-21: Line fit for the time step before and after the second sharp jump indicated in Figure 5-19. In both figure two currents seems to be visible.

shore regions. SeaDarQ is therefore a robust system that can be applied in a broad range of conditions.

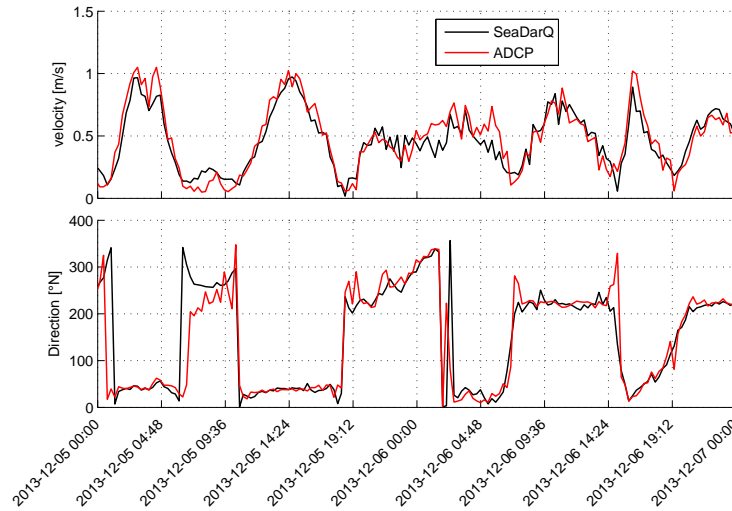


Figure 5-22: SeaDarQ and ADCP output during a storm with wave heights up to 5 meter. The storm conditions do not affect the accuracy of the SeaDarQ output.

5-4 Spatial Analysis

A spatial validation is required before the SeaDarQ output can be used as a measurement system. At the Sand Motor not sufficient velocity data from conventional measurement techniques is available to do a proper spatial validation. It is known that the quality of the radar images decreases for an increasing range. It is therefore expected that the limitations at larger ranges differ from the limitations of the validated point. Another limitation that is not investigated yet is the depth. Near the coast the water depth decreases causing non-linear wave behaviour. The algorithm has proven to give accurate output during storm conditions with wave heights of half the water depth, but there is definitely a limit to the degree of non-linear wave behaviour the algorithm can cope with. Nortek gives 5 meter for the minimum water depth, but no justification of this limit is available.

Six velocity output fields are presented in Figure 5-23 to do a first quick qualitative analysis of the spatial output. The output signal is generally coherent, which gives faith in the reliability of the SeaDarQ output. Different large scale hydrodynamic phenomena can be observed in the output, such as flow field divergence (Figure a), Fresh water plume (Figure b), Eddy (Figure c) and Flow field divergence (Figure d). These phenomena shows the advantages of the this measurement device in comparison with point measurement devices.

SeaDarQ did not derive output points for every single output point. This can be related to several reasons.

- No current output is available for the points on the outer edge of the radar field. It is known that the quality of the radar images decreases for an increasing range. The quality of the images at the outer edge is probably too low to estimate the current.
- No current output is available for the points on the inner edge of the radar field (at the land side). This is probably caused by two shallow water conditions. The waves in this area start to break or become non-linear due to shoaling. The minimum water depth

is according to Nortek 5 meters, but not justification for this limit is available. On the edge of the output field also several outliers are observed. A lower limit for the depth should be defined and used as cut off.

- Figure e and f are the output fields during respectively 4 and 1 m/s wind speed. The lower limit for the wind is depended on the radar range. During low wind speeds on the edge of the output field outliers are observed. These outliers can be eliminated by tightening the quality check of the images or use a filter to eliminate these outliers.

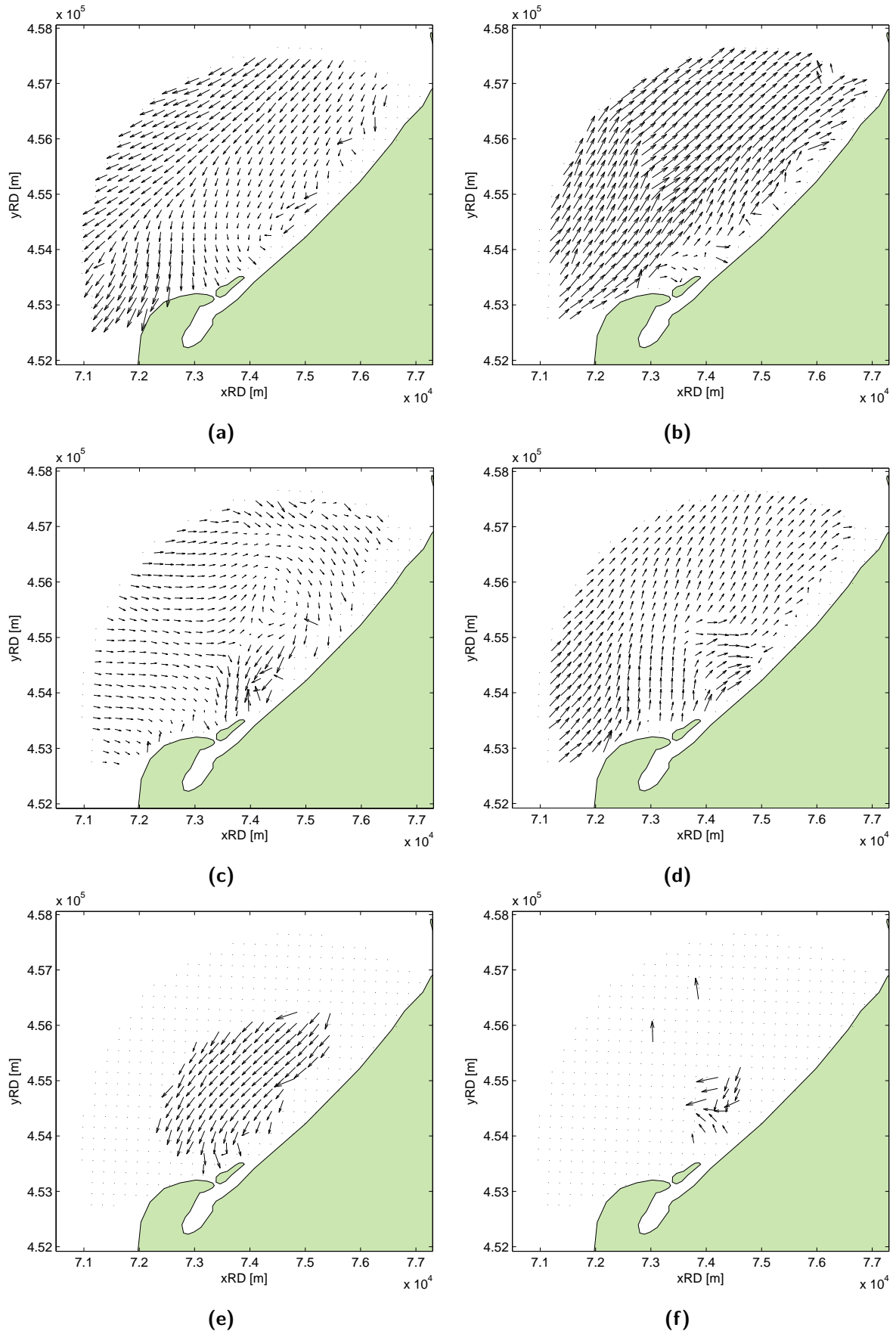


Figure 5-23: Several hydrodynamic phenomena can be captured with SeaDarQ, such as flow field divergence (a), fresh water plume (b), eddy (c), flow field convergence (d). The spatial extent of the output field narrows down during low wind speeds (e) and also outliers are found in the data, which requires filtering and more knowledge about the limitations (f).

Chapter 6

Conclusion

The aim of this research was to investigate if SeaDarQ is able to detect large scale hydrodynamic phenomena. **It is proven that SeaDarQ is able to derive currents from X-Band radar images accurately.** A complete velocity field can be solved due to the spatial extend of the radar images. These velocity fields show beside the tidal movement also large scale hydrodynamic structures.

This main question is answered by performing an algorithm analysis and a case study. The algorithm analysis has resulted in several hypotheses about the accuracy and limitations of SeaDarQ. Subsequently, a case study is done to test these hypotheses. It should be mentioned that the case study only includes one spatial output point of the SeaDarQ velocity field, because only one Acoustic Current Doppler Profiler (ADCP) was available for comparison. This point is located north of the radar at a distance of 1.5 kilometres. The conclusions from the case study are only valid for this point.

The algorithm itself is analysed to investigate how the current is derived from the X-Band radar images. The X-Band radar images contain wave information. This wave information is extracted from the images by performing a 3D Fourier Transformation. The linear dispersion relation is fitted through the contributions of the resulting energy density spectrum to estimate the depth and the current. The linear dispersion relation fitted in an iterative fashion. The depth is first estimated after a current compensation and then the current is estimated after a depth compensation. **It can be concluded that the long wave contributions are excluded from the current fit.** The result of this long wave filtering is that an accurate current estimate does not necessarily require a good estimated depth. The depth on the other hand does depend on the accuracy of the current estimate.

An important question is; what is the valid depth of the estimated current? **The valid depth depends on the wave frequencies used for the current fit.** The ratio between the length of the wave and the depth, which can be expressed with the kd factor, determines the active depth of the wave. Relative long waves are active over a larger depth than short waves. The long wave is there for affected by the current over a larger part of the water column than the short wave. **It can be concluded that the SeaDarQ current output represents a depth averaged surface current.** The exact wave frequencies that are used for the current fit should be known to determine the valid depth. Unfortunately, it is not possible to derive these wave frequencies from the current fit. The two week case study is used

to determine the valid depth by comparing the SeaDarQ output with different depth averaged surface currents from the ADCP and calculating the RMSE, Bias and Correlation factor. **The 3.5 meter depth averaged surface current resulted in the best comparison with an RMSE of 0.187 m/s.** Using a variable depth averaged surface current by selecting the best comparison for each time step improved the comparison to an RMSE of 0.046 m/s, but it is not succeeded to correlate the variable depth to a parameter in the fitting procedure. The influence of the accuracy of the depth estimate is also investigated in the case study. The SeaDarQ algorithm is used to derive the current with a predefined fixed depth of 9 meters. This corresponds to a depth accuracy of ± 1.5 . This analysis is done for one day, December 8th. The RMSE of the original data for this day is 0.088 m/s and from the run with the fixed depth the RMSE is 0.072 m/s. **It can be concluded that a rough depth estimate is sufficient to derive an accurate current estimate.**

The limitations of SeaDarQ regarding the ambient conditions is investigated by comparing the SeaDarQ output with the 3.5 meter depth averaged ADCP output for different conditions. This revealed the following limitations:

- 2 m/s wind speed is required to get enough variance in the backscatters radar signal for the waves to be visible in the images. No SeaDarQ output is available for wind speeds lower than 2 m/s
- Rain induces constant backscatter signal making the waves invisible in the radar images. No SeaDarQ output is available during rainy conditions.
- A minimum wave height is required to capture sufficient wave information in the radar images to fit the linear dispersion relation. The minimum wave height observed in the 2 weeks is 28 cm which is sufficient for accurate SeaDarQ output.
- A minimum wave spreading is required for the fitting procedure to converge to a unique solution. The minimum observed wave spreading is 20 degrees. This is sufficient for an accurate current estimate and a larger spreading does not improve the accuracy.
- Waves are not affected by a current that travels perpendicular to the waves and no current can be estimated in this case. The main current direction, determined by the tide, is often perpendicular to the wave direction in the tide, but this does not affect the current accuracy. The spreading is always sufficient to estimate the current even if the main wave direction is perpendicular to the current.
- SeaDarQ is able to estimate the current accurately also during non-linear wave conditions and non-uniform velocity profiles. The main reason for this is the exclusion of the relative long waves in the current fitting and moreover, the linear dispersion relation is a good estimate in non-linear conditions. The SeaDarQ output is accurate during stratified condition, non-linear velocity profiles and wave heights up to 5 meter.

The spatial output fields show large scale hydrodynamic phenomena. This shows the advantage of the X-Band radar as measurement system. Before the spatial output can be used first a spatial validation should be performed. The limitations and accuracy are probably not constant in space. This still needs to be investigated.

Chapter 7

Recommendations

This thesis includes an description of the SeaDarQ algorithm and a validation of one output point of the SeaDarQ flow velocity field. Also the spatial pattern is briefly analysed to conclude what kind of hydrodynamic phenomena can be detected with SeaDarQ. The SeaDarQ output is very accurate for the considered output point and the coherence in the flow velocity field gives faith in the complete output field, but it is expected that the accuracy and limitations differ spatially. Also the valid depth for the derived currents is not know exactly. The following recommendations are done to extend the validation spatially and to improve the knowledge about processes in the algorithm.

- The algorithm description made during this research focuses on the current estimate and is based personal discussion with J. Perez. A full detailed description of the whole algorithm based on the code will help to determine the influences of the preprocessing phase and the aliasing filter.
- The case study is done for one point in space and the spatial differences in the output accuracy is therefore not researched. It is known from literature that the backscatter intensity differs spatially so this should definitely be investigated as well.
- The hydrodynamic conditions at the Sand Motor are quite complex. A first validation of the SeaDarQ output should be done at a less complex hydrodynamic location to investigate the output accuracy at a "ideal" situation. Afterwards, a validation in more complex conditions can be done to investigate the influence of different hydrodynamic structures such as a density driven current.
- The near surface current is most important to validate the SeaDarQ current output. Drifters can be used to measure the surface current. Alternatively, a downward looking Acoustic Current Doppler Profiler (ADCP) located near the surface can provide current information closer to the water surface. This can be used to get a better idea of the valid depth for the current output.
- Testing SeaDarQ at a location that can be modelled very accurately would provide spatial information to research the spatial influence on the output accuracy and to get a better idea of the valid depth for the current output.

- The line fitting is not totally understood. Artificial input can improve the knowledge about the current fitting. This artificial input should contain waves that are influenced by different current magnitudes and directions to understand which waves are ultimately used to fit the current.
- Another fitting procedure for the current can be used to get a better idea of the wave frequencies that are used for the current fit. The big advantage of SeaDarQ is its insensitivity to the accuracy of the depth. This is reached by excluding the relative long waves from the current fit. This knowledge can be used to develop a fitting procedure in the k_x, k_y, ω -space with the same accuracy and robustness. The advantage of fitting in this space would be that it becomes clear which wave frequencies are used for the current fit. This can be translated to a valid depth for the fitted current.

Bibliography

- Allen, J. (1977). Short-term spectral analysis, and modification by discrete fourier transform.
- Atanassov, V., Rosental, W., and Ziemer, F. (1985). Removal of ambiguity of two-dimensional power spectra obtained by processing ship radar images of ocean waves.
- Bell, P. (2008). Mapping shallow water coastal areas using a standard marine x-band radar. In *Proceedings of Hydro8 Conference*.
- Borge, J. N., Reichert, K., and Dittmer, J. (1999). Use of nautical radar as a wave monitoring instrument. *Coastal Engineering*, 37:331–342.
- Borge, J. N., Rodriguez, G., Hessner, K., and Gonzales, P. (2004). Inversion of marine radar images for surface wave analysis. *Journal of Atmospheric and Oceanic Technology*., 21:1291 – 1300.
- Borge, J. N. and Soares, C. (2000). Analysis of directional wave fields using x-band navigation radar. *Coastal Engineering*, 40:375–391.
- Dittmer, J. (1995). Use of marine radars for real time wave field survey and speeding up the transmission/processing.
- Hessen, K. and Bell, P. (2009). High resolution current & bathymetry determined by nautical x-band radar in shallow waters. *Oceans 2009 - Europe*.
- Holthuijsen, L. (2007). *Waves in Oceanic and Coastal Waters*. Cambridge University Press.
- Mattie, M. and Harris, D. (1979). A system for using radar to record wave direction.
- Nortek (2013). Seadarq wave processing. Presentation about the SeaDarQ algorithm.
- Oudshoorn, H. (1960). The use of radar in hydrodynamic surveying.
- Press, W., Teukolsky, S., Vetterling, W., and Flannery, B. (1986). *Numerical Recipes: The Art Of Scientific Computing*. Cambridge University Press.
- Reichert, K., Hessner, K., Borge, J. N., and Dittmer, J. (1999). Wamos ii: A radar based wave and current monitoring system.

- Rutten, J. (2013). Marine x-band radar derived wave field quality on an ebb tidal delta. M.sc. thesis, Universiteit Utrecht.
- Swinkels, C., Peters, H., and Heesen, J. (2012). Analysis of current patterns in coastal areas using x-band radar images. *Coastal Engineering Proceedings*, currents.39.
- Valenzuela, G. (2012). Theories for the intercation of electromagnetic oceanic waves - a review. *Boundary-Layer Meteorology*, currents.39.
- Young, I., Rosenthal, W., and Ziemer, F. (1985). A three-dimensional analysis of marine radara images for the determination of ocean wave directionality and surface currents. *Journal of Geophysical Research*, 90:1049–1059.
- Ziemer, F. (1991). Directional spectra from shipboard navigation radar during lewex.
- Ziemer, F., Rosenthal, W., and Carlson, H. (1983). Measurements of directional wave spectra by ship radar.